Structures 70 (2024) 107681

Contents lists available at ScienceDirect

Structures

journal homepage: www.elsevier.com/locate/structures

Utilization finite element and machine learning methods to investigation the axial compressive behavior of elliptical FRP-confined concrete columns

Chen Yue [a], Haytham F. Isleem [b,*], Diyar N. Qader [c], Alireza Mahmoudian [d], Tian Weiming [e], Pradeep JANGIR [f,g,h,k], Arpita [i], Asmaa Y. Hamed [j]

[a] College of Management, Hunan University of Information Technology, Changsha, Hunan province, China
[b] Jadara University Research Center, Jadara University, Irbid, Jordan
[c] Civil Engineering Department, University of Kirkuk, Kirkuk, Iraq
[d] Department of Civil Engineering, Shahid Rajaee Teacher Training University, Tehran, Iran
[e] College of Management, Hunan University of Information Technology, Changsha, Hunan Province, China
[f] University Centre for Research and Development, Chandigarh University, Gharuan, Mohali 140413, India
[g] Department of CSE, Graphic Era Hill University, Dehradun 248002, India
[h] Applied Science Research Center, Applied Science Private University, Amman 11931, Jordan
[i] Department of Biosciences, Saveetha School of Engineering. Saveetha Institute of Medical and Technical Sciences, Chennai 602105, India
[j] Construction and Building Department, The Higher Institute of Engineering and Technology Luxor, Egypt
[k] Adjunct Professor, Department of CSE, Graphic Era Deemed To Be University, Dehradun, 248002, Uttarakhand, India

ARTICLE INFO

Keywords:
Elliptical sections
FRP composite columns
Confinement efficacy
Concrete damage plasticity model
Stress-strain response
ML algorithms

ABSTRACT

Nowadays, elliptical sections are among the geometric shapes that are becoming more and more popular in the architecture world. Finite element analysis (FEA) software, such as ABAQUS, is used to simulate elliptical concrete columns confined with fiber reinforced polymer (FRP) jackets based on experimental data published in the literature. The validity of the finite element modeling (FEM) approach was confirmed by comparing it to experimental data obtained from 45 specimens in existing studies, demonstrating a favorable agreement. Additionally, a parametric study was also carried out, which included simulating 40 more specimens, resulting in a total of 85 specimens for analysis. The effect of various test variables such as sectional aspect ratio, the amount of FRP layers, and concrete strength on the elliptical column's behavior is investigated. The axial compressive strength is predicted using current models from the literature. The outcomes revealed that the higher unconfined concrete strength decreased FRP confinement efficacy. Insufficient confinement with post-peak softening is more likely in FRP-confined high strength concrete columns, especially if the confinement was not stiff enough. Also, by adding more FRP layers, the stress and strain capabilities of elliptical concrete columns confined with FRP composites are improved. Physical experiments require a significant investment of time and resources, but they can produce valuable results. Finite element analysis, on the other hand, depends heavily on the modeler's competence and can minimize the number of experiments required by employing computer simulation, but it also requires high computer settings. In recent years, there has been a major advancement in the usage of machine learning (ML) algorithms in the applications of FRP composites with different concrete components. Taking

Abbreviations: f_{cc}, Peak strength of confined concrete; ε_{cc}, Strain corresponding to f_{cc}; f_{co}, Peak strength of unconfined concrete; ε_{co}, Strain corresponding to f_{co}; E_f, Young's modulus of FRP; t_f, Total thickness of FRP layers; 2a, Longer side of elliptical column; 2b, Shorter side of elliptical column; Ag, Gross cross-sectional area of elliptical column; c, Confinement stiffness ratio of FRP jacket; H, Height of elliptical column; ANN, Artificial neural network; BP-ANN, Back propagation- artificial neural network; C3D8R, Eight-node hexagonal solid 3-D element; CFRP, Carbon fiber reinforced polymer; CV, Cross validation; DSTC, Double skin tubular column; DT, Decision tree; ET, Expression tree; FCHC, FRP-confined hollow concrete; FCSC, FRP-confined solid concrete; FEA, Finite element analysis; FEM, Finite element modeling; FRP, Fiber reinforced polymer; GB, Gradient boosting; GEP, Genetic expression programming; GFRP, Glass fiber reinforced polymer; GI, Gini impurity; GRNN, Generalized regression neural network; HSC, High strength concrete; MAE, Mean absolute error; MAPE, Mean absolute percentage error; ML, Machine learning; NSC, Normal strength concrete; PR, Polynomial regression; R2, Coefficient of determination; RF, Random forest; RMSE, Root mean squared error; S4R, Four-node reduced integration shell element; SHAP, SHapley additive explanations; XGB, XGBoost.

* Corresponding author.
E-mail addresses: chenyue73@hnuit.edu.cn (C. Yue), mps565@york.ac.uk (H.F. Isleem), diyar.nasih@uokirkuk.edu.iq (D.N. Qader), amahmoudian1997@sru.ac.ir (A. Mahmoudian), tianweiming@hnuit.edu.c (T. Weiming), pkjmtech@gmail.com (P. JANGIR), apyjangid@gmail.com (Arpita), dr_asmaa11@adj.aast.edu (A.Y. Hamed).

https://doi.org/10.1016/j.istruc.2024.107681

this into consideration, this investigation is extended to estimate the compressive strength of elliptical FRP-confined columns using four tree-based ML algorithms including Decision Tree, Random Forest, Gradient Boosting and XGBoost. The XGBoost model achieved the highest predictive accuracy with the R^2 values of 0.95 for both the compressive strength and axial strain targets.

1. Introduction

Compared to circular columns, elliptical columns offer the advantage of having different bending capacities in the major and minor axes, making it easier to tailor them to specific design needs [1]. Moreover, the elegant shape of elliptical columns adds aesthetic value to structures [2]. An additional benefit of elliptical columns is that, in contrast to rectangular columns, the concrete in them is better confined because of a more uniform confining stress distribution [3] The compressive behavior of elliptical columns has been the subject of numerous investigations [4]. Several variables have been well investigated and documented, such as sectional aspect ratio, concrete strength, and load pattern [5–10]. Even though it is difficult to analytically estimate the axial performance of elliptical FRP-confined columns, a number of important design-oriented models have been proposed for use in design practice. A design-oriented method for forecasting the stress-strain responses of FRP-confined elliptical columns was presented by Campione and Cucchiara [7]. The laboratory findings of eight elliptical columns (peak strength of unconfined concrete f_{co} range: 36.6 to 39.0 MPa) published by Teng and Lam [11] were used to validate the model's performance. A reliable and straightforward stress-strain model for circular columns confined with FRP jackets has been developed by Teng et al. [12], which may be used in design practice. Their previous model [13] [13] was utilized as a reference for circular-shaped columns wrapped with FRP layers. Their model was calibrated using numerical analysis in conjunction with the outcomes of their own experiments. Subsequent research [12] have addressed and corrected certain shortcomings in their earlier work [11]. Then, using previously published research by Wei and Wu [14]on various concrete shapes such as square, rectangular, circular, and elliptical concrete columns that were significantly wrapped by FRP layers, Cao et al. [15] established a stress-strain model of columns wrapped with FRP jackets with cross-sectional unification. The elliptical-shaped columns were regarded as rectangular-shaped columns with distinct corner radii. Chen et al. [3] established a novel design-oriented model featuring a strain shape factor. This model can accurately forecast the stress and strain capacities of FRP-confined columns in elliptical sections across a significantly wider range of peak strengths of unconfined concrete (32.6 to 72.4 MPa). They were able to reduce their model to a well-known model for FRP-confined columns with circular shapes with greater ease than the previous models mentioned above.

Concrete undergoes notable improvements in compressive strength and ductility when it is subjected to lateral confinement, which can involve active, passive, or hybrid confinement processes. Because of this, confined concrete has been used in columns much more frequently in the last few decades, particularly in buildings intended to withstand seismic loads. Lateral confinement to concrete in columns has been accomplished by a variety of methods, including FRP jackets and transverse steel bars [16–21]. In recent several years, FRP jacketing technique has been applied to both elliptical and rectangular concrete columns to improve their load-carrying capacity and provide excellent resistance against deformation and failure [22–25]. Elliptical concrete columns have been found to exhibit superior strength and ductility when subjected to FRP confinement. By minimizing the possibility of an early failure from axial compression loads, the application of FRP confinement increases the concrete strength in the columns [26–28]. Because FRP confinement lessens the possibility of collapse during earthquakes and other disasters, which can also boost the safety of elliptical concrete columns. For instance, the circular/elliptical geometry of the FRP composites allows for uniform distribution of lateral stress, which effectively increases the confinement efficiency of the concrete core and improves the overall performance of columns [29–32]. Twenty-four elliptical-shaped FRP-confined columns were subjected to axial compressive tests by Chen et al. [3]. There was discussion of the implications of high-strength concrete, cross-sectional aspect ratio, and FRP jacket. The results of the tests demonstrated that confined concrete stress and strain capacities increased with increasing FRP jacket confinement. Because high-strength concrete was employed and the aspect ratio increased, the FRP confining pressure was not distributed uniformly, which affected the axial performance of the inner concrete. Furthermore, based on an experimental and FE analysis, Teng et al. [12] developed a stress-strain model for elliptical concrete columns wrapped with FRP layers. The accuracy of a FEA modeling for elliptical columns was validated with their own test results. The ultimate axial stress, ultimate axial strain, and jacket hoop rupture strain of FRP-confined elliptical columns are significantly influenced by the aspect ratio and thickness of FRP layers. Furthermore, they concluded that as the cross-sectional aspect ratio and jacket thickness decreased, the confinement effectiveness of FRP jackets decreased as well.

The FEA approach is widely recognized for its ability to forecast the performance of structural components with great versatility. It is also a highly effective tool for modeling the overall behavior of confined concrete. Because this process can record complex stress variations in the concrete, it is capable of accurately imitating the performance of confined concrete [30,33]. The application of finite element analysis on concrete columns in elliptical sections subjected to external loading is reported by Isleem et al. [34,35]. They examined the impact on axial load-carrying capacity of elliptical shapes of confined concrete columns confined with steel tube and carbon fiber reinforced polymer (CFRP) layers. It has been concluded that the section should definitely be wrapped with CFRP jackets if the aspect ratio is larger. Chen et al. [36] studied the compressive strength of an elliptical FRP-concrete-steel double skin tubular column (DSTC). Two sets of reference specimens, FRP-confined solid concrete (FCSC) and FRP-confined hollow concrete (FCHC) specimens, were used to compare the outcomes. The DSTC's confined concrete strength increases by 20 % to 55 % when compared to the equivalent elliptical FCSC with the same column diameters and FRP confinement level. One explanation could be that a hollow steel tube was used in place of the elliptical FCSC's less efficient confinement zone. With high-strength concrete, the behavior of elliptical DSTC could not be directly predicted by the current model. Combining FE analysis with plasticity-based models has proven to be an efficient way to capture the deformation and strength properties of both typical and high-performance concrete members [17,37–39]. Accurate material parameter calibration is a prerequisite for accurate FEM results [33,40]. A key element of a plasticity model is the dilation property of the concrete, or the relationship between lateral and axial strain. In the case of non-uniform confinement, where an "effective" value is used to represent uniform confinement, or of uniform confinement, where the confinement pressures in the two lateral directions are equal, a correlation of this kind has been found for passively confined concrete, such as FRP-confined columns [41].

Compressive strength is the main mechanical property of an elliptical CFRP/glass fiber reinforced polymer (GFRP)-confined concrete column. It is important for the precise design of elliptical columns to guarantee structural stability. Researchers frequently employ experimental and FE approaches to assess the overall performance of elliptical columns confined with FRP layers under loads in order to better understand how

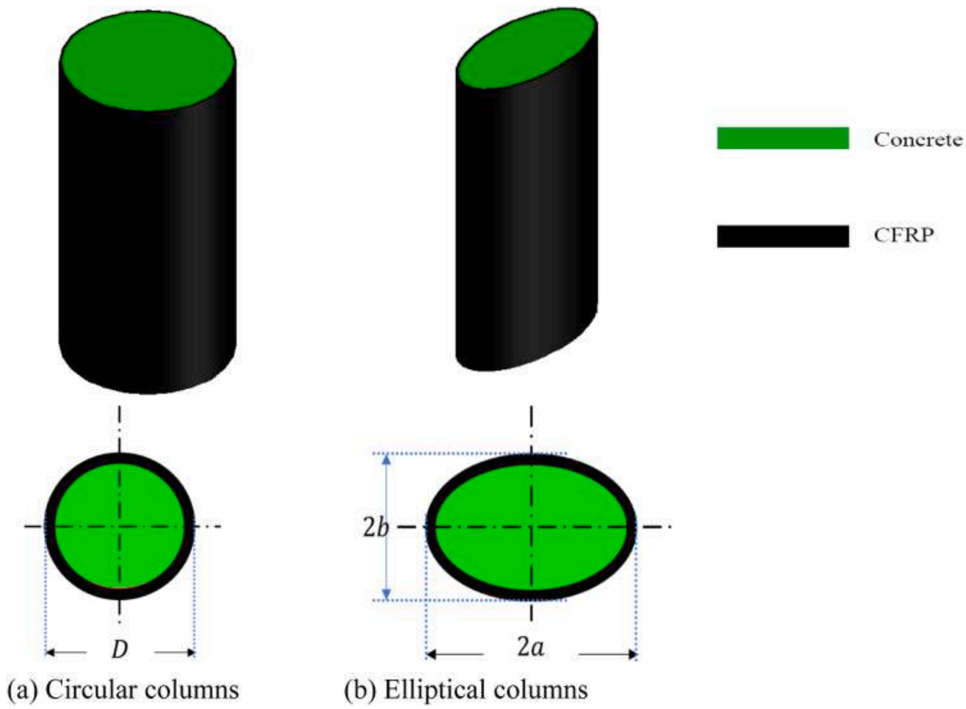

Fig. 1. Numerically simulated column specimens in the present study.

these columns behave [2,3,12,42]. Although physical experiments need a lot of resources and time, they can yield insightful results. However, finite element analysis, which relies significantly on the modeler's skill, might decrease the number of tests needed by using computer simulation; however, it also necessitates high computer settings [43]. In the last several years, there has been a significant increase in the use of ML techniques in the field of FRP composites with different concrete components. Machine learning-based models, which are data-driven and able to capture deeper correlations and patterns in the data, may be more reliable than design-oriented models for complex and nonlinear systems. Because ML approaches can learn from any data and generate predictions, they are very adaptable to a wide range of materials, geometries, and stress conditions. In general, ML is used to increase estimation accuracy by giving the computer enormous amounts of datasets in an effort to maximize accuracy. Several studies have utilized various models such as artificial neural networks (ANN), back propagation ANN (BP-ANN), generalized regression neural network (GRNN), CAT boost algorithm, and XG boost algorithm to estimate the compressive stress of FRP-confined concrete. For instance, Naderpour et al. [44] investigated the ANN model's performance in predicting FRP concrete's compressive strength. Similarly, Huang et al. [45] developed a hybrid model of BP-ANN to forecast the compressive stress of FRP-reinforced concrete exposed to various temperatures. Alam and Gazder [46] developed a GRNN model to predict FRP-reinforced concrete shear strength. In another study, Kim et al. [47]presented a CAT boost algorithm model that accurately predicts the interfacial bonding of the FRP-reinforced concrete using experimental results. Moreover, the XG boost algorithm predicts the interfacial bonding of the FRP-reinforced concrete. Additionally, Sangeetha and Shanmugapriya [48] estimated the axial compressive strength of circular-shaped concrete columns that were externally confined using various GFRP materials using ANN. The number of GFRP sheets, the type of GFRP jacket, and the curing time were among the variables. Tests were conducted on twenty-one cylindrical specimens under compression until they failed. They came to the conclusion that the concrete columns with GFRP confinement increased the compressive strength by 30 %. More applications of ML algorithms in concrete structures can be found in literary works [49–51].

Notably, no prior research has used ML techniques to predict the compressive stress of elliptical-shaped concrete columns wrapped with CFRP/GFRP jackets. Using FEA and ML modeling with the assistance of previously published experimental data from the literature, the effect of aspect ratio, concrete strength (normal strength concrete (NSC) and high strength concrete (HSC)), and thickness of FRP layers is investigated in the current study. Therefore, the primary aim of this research included three objectives: (a) to compare the simulated stress and strain data generated by ABAQUS software with the test data of the elliptical FRP-confined concrete columns reported in the literature (b) to conduct a numerical investigation into how the aspect ratio, amount of CFRP/GFRP layers, and concrete strength affect the compressive behavior of elliptical FRP-confined concrete columns; (c) to develop ML models to predict the compressive strength of elliptical-shaped columns wrapped with CFRP/GFRP layers. It is to be noted that these tests did not consider the effect of internal steel reinforcing bars or tubes. Both circular and elliptical concrete columns confined with FRP wraps are considered in this investigation (see Fig. 1.).

2. Research significance

FRP composites have been extensively utilized in engineering practices, particularly in FRP wrapping or tubes, as external confinement systems for concrete columns with various cross-sectional shapes and load conditions. Previous works, including experimental and numerical studies, have provided valuable insights into the mechanism of FRP-confined concrete columns. The majority of research in the literature focuses on experimental investigations with concrete columns that are square, circular, and rectangular and are confined with FRP jackets; theoretical and simulation studies are carried out independently.

Previous research on FRP composite columns has focused on strength and numerical modeling; more research must be done on forecasting the strength characteristic of elliptical and rectangular FRP-confined columns. Machine Learning approaches are now adopted widely in various applications of engineering fields. However, ML methods still require elaborate studies to forecast the strength characteristics of elliptical-shaped columns wrapped with FRP sheets (CFRP and GFRP). The

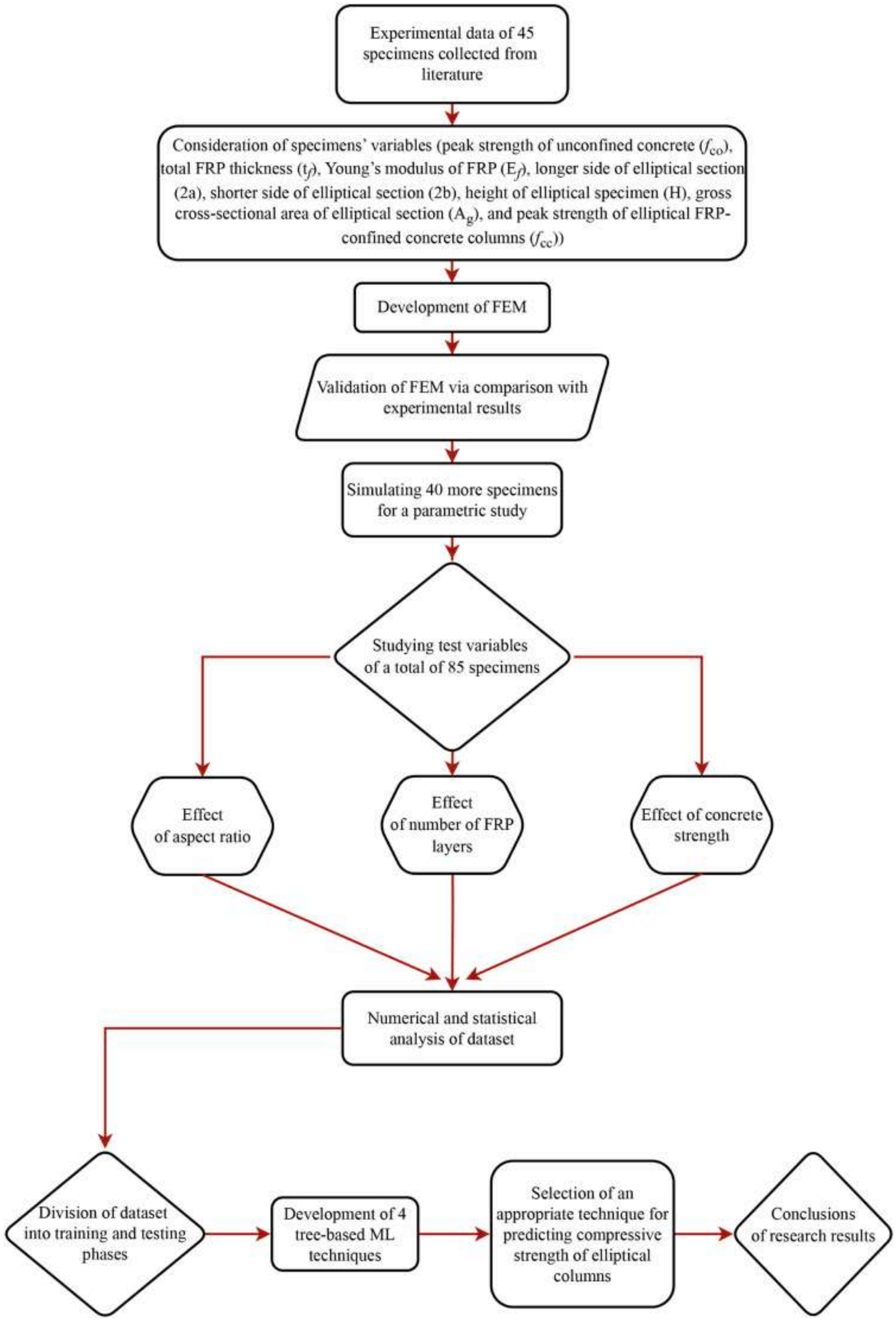

Fig. 2. Flowchart of research methodology.

models that have taken into account FRP's simultaneous influence when estimating the compressive stress of FRP-confined columns are described in this work. Additionally, eight input variables, including peak strength of unconfined concrete, the total thickness of FRP, E_f, $2a$, $2b$, H, A_g, and f_{cc} as a target variable, were used to develop four tree-based models based on 85 validated experimental and finite element data in order to estimate the axial performance of concrete columns confined with FRP layers. The eight input variables used in our study were chosen based on an in-depth investigation of the literature as well as the specific criteria necessary to fully describe the behavior of elliptical FRP-confined concrete columns. These variables were selected based on their significance in influencing the axial compressive behavior of such columns. The research methodology adopted for this investigation is depicted in Fig. 2.

The criteria used to choose parameters for the 40 column specimens in the finite element parametric study required a careful review of previous literature to pinpoint important factors that were frequently looked at in studies that investigated elliptical FRP-confined concrete columns. In order to guarantee that these variables had a substantial impact on the axial compressive behavior of elliptical FRP-confined concrete columns, priority was given to parameters that have been extensively studied in the field. The selection procedure took into account factors that directly affect the behavior of these columns, highlighting their importance from an engineering perspective as well as

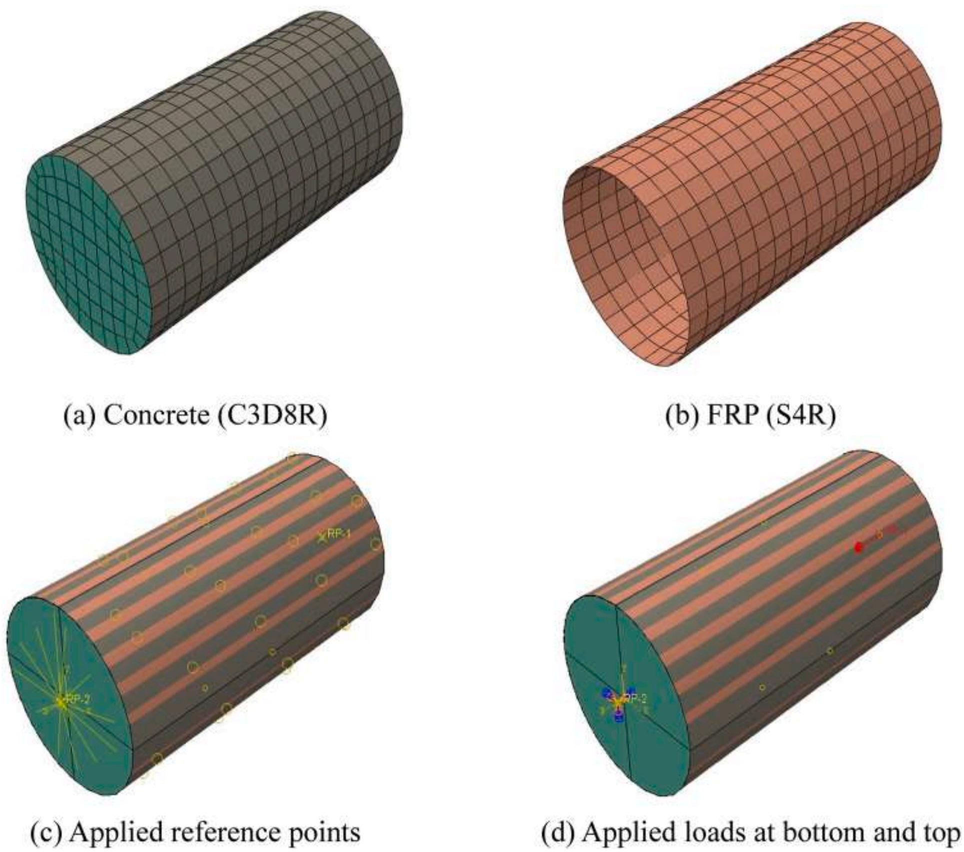

Fig. 3. Finite element type of elements, meshing and applied loads.

their connection to the objectives of the study. Parameters were selected in such a way as to enable the development of a cohesive dataset useful for ML and FEA modeling while preserving consistency between experimental and numerical data.

3. Experimental database

Engineers and architects find elliptical concrete columns particularly appealing due to their distinct benefits. Additionally, CFRP/GFRP jacketing can improve the peak strength and ultimate axial strain of concrete columns in elliptical shapes. The FEM approach is verified through a comparison with the results of 45 experimental specimens from four previously published works available in the literature [3,12,42,52] via ABAQUS software. To expand the investigation, forty more simulated specimens are considered as a parametric study. In total, 85 specimens are collected for further studies using Machine Learning methods with eight variables: peak strength of unconfined concrete (MPa), height of the specimens (mm), cross-sectional area of the specimens (mm^2), Young's modulus of the FRP (MPa), thickness of the FRP layer (mm), elliptical size (longer direction (mm), shorter direction (mm)), and peak strength of elliptical FRP-confined concrete columns (MPa). The details of 85 experimental and simulated data are reported in Annexure I.

4. Finite element simulations

4.1. General description

Numerical models were developed and analyzed utilizing ABAQUS [53]. In this investigation, the chosen elements for the representation of concrete and FRP ply were C3D8R and S4R, respectively. The top and bottom of the column were coupled kinematically. The boundary conditions at both ends of the column were established through two reference points (RP1, RP2). To ensure a consistent transfer of axial load, these reference points were positioned at the midpoint of each end of the column, as depicted in Fig. 3-c and d. To achieve uniform compression, RP1 was linked to the upper surface of the top end of column, where an axial displacement force was applied along the Z-axis. In this configuration, all degrees of freedom were constrained except for Uz, which denotes axial displacements in the Z direction. This setup enabled accurate measurement of the axial load in relation to the displacement responses of the specimens. In the other hand, the fixed-end conditions at the bottom reference point (RP2) ensured stability and eliminated any lateral movement, thereby maintaining the columns remained in place during testing. To mitigate velocity and lower kinetic energy levels, step smoothing was implemented during the use of Abaqus/Explicit for simulating the dynamic problem, aligning with static analysis recommendations. Mesh convergence studies were conducted for the model. Hexagonal elements with a structured mesh technique were used for the concrete elements, while quadrangle shapes were used for the FRP wrapping to strike a good balance between solution accuracy and computational time. A perfect connection between the FRP jacket and the concrete was achieved by employing the "surface-to-surface" tie interaction contact model option in ABAQUS software, which simulated a no-slip condition. The master surface for the tie constraint was designated for the FRP jacket, while the slave surface was designated for concrete.

4.2. Material Modeling

4.2.1. FRP modeling

The elastic properties of FRP sheets can be defined in ABAQUS using the "Engineering Constants" material type. This allows for the specification of the longitudinal and transverse elastic moduli, the rigidity

Table 1
Properties of CFRP and GFRP tested by [54].

	Thickness of one layer (mm)	Elasticity properties (MPa)			Poisson's ratio			Shear modulus properties (MPa)		
		E_1	E_2	E_3	μ_{12}	μ_{13}	μ_{23}	G_{12}	G_{13}	G_{23}
CFRP	0.167 −0.171	235,000	23,500	23,500	0.3	0.3	0.3	5405	5405	5405
GFRP	0.167 −4.85	90,000	900	900	0.3	0.3	0.3	3270	3270	3270

moduli, and the Poisson coefficients. In the case of unidirectional fibers, it is possible to specify only E_1 and assign very small values to the other elastic parameters to minimize interaction with other directions. The mechanical characteristics and plasticity parameters of the confining CFRP and GFRP materials used in the numerical analysis verification [54] are reported in Table 1. The thicknesses of CFRP used in this study are 0.167 mm and 0.171 mm, while the thicknesses of GFRP used are 0.167 mm, 0.354 mm, 2.840 mm, 2.890 mm, 3.140 mm, 3.150 mm, 4.260 mm, 4.410 mm, 4.430 mm, and 4.850 mm, respectively.

4.2.2. Concrete modeling

The modeling of concrete to assess the confinement effects provided by FRP wrapping represents a critical phase in the finite element method (FEM) definition process, directly influencing the precision of the outcomes. Within the Abaqus software, two types models are available for characterizing concrete behavior: the Drucker-Prager (D-P) plasticity model [55]and the Concrete Damaged Plasticity model (CDP) [56]. In recent decades, numerous investigations have been conducted to explore the impact of material parameter definitions. To achieve a closer alignment with experimental data, various formulations for calibrating the parameters related to concrete properties under FRP confinement have been proposed [17,38,39]. In this study, the CDP model is proposed for simulating confined concrete within the Abaqus framework. It considers both tensile cracking and compressive crushing of concrete under axial stress conditions. The response of concrete is characterized by the damage variable, yield criterion, flow rule, and the rules governing hardening and softening. By defining the plasticity parameters, including the dilation angle ψ, the ratio (f_{bo}/f_{co}), the flow potential eccentricity e, the viscosity parameter μ, and the ratio K_c relevant to the yield function [57]. While the flow potential eccentricity (e) remains constant at the default value ($e = 0.1$) [58], other parameters can significantly impact analysis results. The viscosity parameter μ characterizes damage propagation and affects tensile strength. A value of μ equal zero is suggested [37]. An empirical equation for the (f_{bo}/f_{co}) factor fits various cases [59], including confined specimens with different concrete strengths and confinement ratios. This equation was proposed by Hany et al. [37] and Tao et al. [60] to characterize the behavior of concrete with FRP-confinement. Based on the results of a regression analysis performed for a large number of specimens, an empirical relationship to obtain K_c is defined in [30]. The dilation angle (ψ) is crucial as it affects lateral confinement pressure and strength properties. Various formulations are available [37,60] for approximating the dilation angle, such as the equation proposed by Hany et al. [37] for circular cross-section which considers the unconfined concrete strength f_{co} and the radial stiffness ($Kl = \frac{2E_f t_f}{D}$) of the FRP sheets and can be calculated as follow:

$$\psi = -1.4587\frac{K_l}{f_{co}} + 57.296 \text{For} 0 \leq \frac{K_l}{f_{co}} \leq 40 \quad (1)$$

Based on similar studies by Isleem et al. [27,61,62] on non-circular concrete columns confined by FRP and steel tubes, new models to predict the values of dilation angle were proposed, i.e., elliptical and rectangular sectioned columns confined by FRP. Additionally, the thickness of FRP tubes can vary based on the number of fiber layers, which makes it difficult to control resin volume during manufacturing. This results in significant differences in elastic modulus across different thickness categories. Increasing the number of FRP layers and the cross-sectional aspect ratio applies more pressure on the concrete core, causing it to change from dilation to contraction behavior, which needs to be considered in modeling.

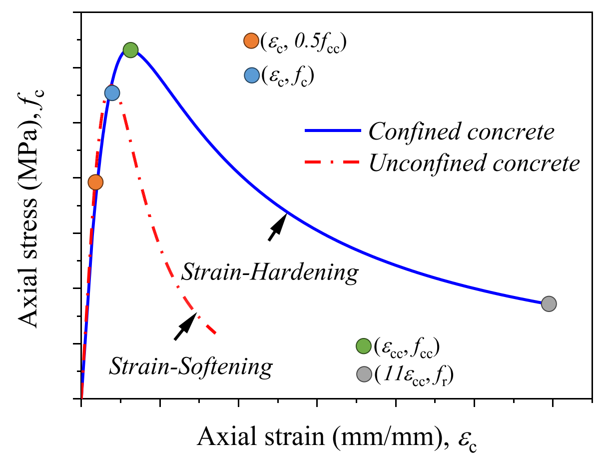

Fig. 4. Stress-strain curve for both confined and unconfined concrete.

Through a statistical analysis, the following Eq. (2) is obtained with the coefficient of determination (R^2) of 85 %.

$$RF = 1.28213 \times \left(\frac{2a}{2b}\right)^{-0.6849} \times \left(0.001\frac{t_f \times E_f}{f_{co}}\right)^{-0.6849} \quad (2)$$

where, RF is a reduction factor of E_f, $2a$ (mm) is the longer side of the elliptical cross section, $2b$ (mm) is the shorter side of the elliptical cross section, as shown in Fig. 1, t_f is the thickness of FRP layer (mm), E_f (MPa) is the elastic modulus of FRP jacket, and f_{co} (MPa) is the peak strength of unconfined concrete.

It is evident from the above equation that an increase in the confinement stiffness offered by the FRP leads to a decrease in the dilation angle. Similarly, an increase in the aspect ratio results in a significant reduction of the dilation angle, which corresponds to the pronounced decrease in confinement observed in the elliptical cross-section.

A theoretical stress-strain model has been developed to enhance the comprehension of the behavior of FRP- confined concrete columns. The stress-strain relationship of confined concrete is not solely determined by the concrete strength grade and confinement stress. The development of strain in the confining material, concrete strength, concrete composition, microstructure, and wet packing density all influence the stress-strain relationship of confined concrete. This model is based on various studies referenced in Ref [63–70]. It consists of four main elements: the interaction between the steel tube and concrete, accounting for the debonding effect; a precise equation for the hoop strain; a model for the behavior of confined concrete accounting for stress-path dependency; and a three-dimensional stress-strain model for the steel tube.

The compression stress response of concrete (σ_c) was determined by Eq. (1) [35,52]. The elastic response of the confined or unconfined concrete in the current FE simulation begins at a stress value of 50 %, and the stress-strain response that is achieved terminates at the

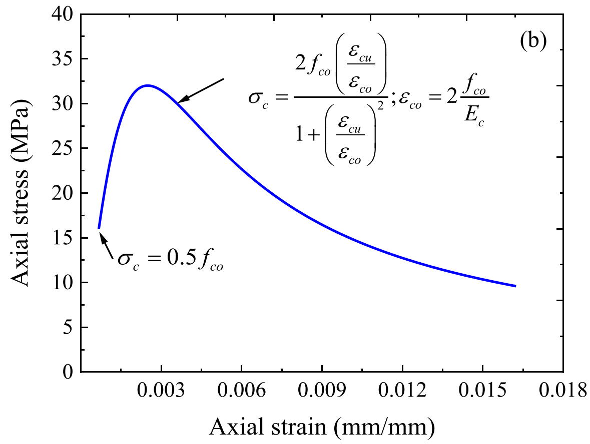

Fig. 5. Stress-strain curve of unconfined concrete under compression.

unconfined concrete's compressive strain at failure, which is represented by the ultimate strain (ε_{cu}).

$$\sigma_c = \frac{2f_{co} \times \left(\frac{\varepsilon_{cu}}{\varepsilon_{co}}\right)}{1 + \left(\frac{\varepsilon_{cu}}{\varepsilon_{co}}\right)^2} \tag{3}$$

where, f_{co} is the peak strength of unconfined concrete (MPa), ε_{co} (mm/mm) is the strain corresponding to f_{co}, and ε_{cu} is the ultimate compressive strain. Therefore, ε_{co} and ε_{cu} are calculated using Eqs. (2) and (3), respectively. Fig. 5 illustrates the mathematical models for generating the compressive stress-strain response of unconfined concrete [71,72].

$$\varepsilon_{co} = 0.0014 \quad \left[2 - e^{\left(-0.024 f_{cm}\right)} - e^{\left(-0.140 f_{cm}\right)}\right] \tag{4}$$

$$\varepsilon_{cu} = 0.004 - 0.0011\left[1 - e^{\left(-0.0215 f_{cm}\right)}\right] \tag{5}$$

5. Results and discussion

5.1. Comparison of experimental and FEM results

The verification of FEM approach is done through the comparisons with 45 experimental results available in the literature [3,12,42,52]. There are various benefits to these comparisons, including lower expenses, less use of resources, preservation of natural resources for later use, etc. (Fig. 6.a, b) compares experimental and FEM results from [3, 52]. It can be noted that 8 experimental results were collected from [3], divided into two batches, and arranged from higher to lower axial load and axial strain, while one experimental result was obtained from [52]. Additionally, Fig. (6.c) presents the experimental and FEM data of 4 specimens, that were gathered from [12]. Lastly, the comparison of experimental and FEM results of 8 specimens collected from [42] is depicted in Fig. 7.d.

The majority of axial load-axial strain curves in Fig. 6 exhibit a monotonically ascending response (i.e., without a descending trend) with two-segment behavior which can be classified as being heavily confined, except for specimens D8, in Fig. (6.d). In heavy confinement scenario, peak and ultimate stress states closely align. In semi-heavy confinement, some curves show a gradual response increase with a slight axial load reduction, indicating that the FRP jacket lacks the rigidity to prevent brittle concrete cracking. Conversely, some specimens display a decline after peak stress, indicating insufficient confinement when unconfined concrete strength exceeds ultimate strength. Such confinement levels should be avoided in design. Additionally, higher unconfined concrete strength reduces confinement effectiveness at a given FRP level, making high-strength concrete (HSC) columns more prone to insufficient confinement and post-peak softening if the FRP lacks adequate stiffness [3,73,74]. Overall, there is a strong correlation between experimental and numerical relationships of axial load and strain.

5.2. Stress-strain behavior

Fig. 7 depicts stress and strain values at different positions for the 45 experimental results obtained from the aforementioned published works in the literature [3,12,42,52]. The literature reports similar effects for stress and strain results [75,76]. The ultimate axial stress and corresponding axial strain increase with increase number of the FRP. However, the non-uniform distribution of FRP confining pressure negatively impacts the axial behavior of elliptical FRP-confined concrete columns. High-strength concrete is stiffer and has less extensive concrete crack development, resulting in a longer lag between the development of axial strain and confining strain and stress.

5.3. Effects of test variables

The impacts of different test variables including three main parameters such as concrete strength, number of FRP layers, and sectional aspect ratio on the strength and strain enhancements for a total of 85 experimental and simulated specimens are presented in the following subsections.

5.3.1. Effect of variation in concrete strength

Fig. 8 illustrates the relationship between concrete strength and the strength enhancement ratio for experimental specimens (A1 to A16) with a strength of 72.4 MPa and simulated specimens (A17 to A32) with a strength of 50 MPa, categorized by aspect ratios of 1.0, 1.3, 1.7, and 2.0. The data shows an inverse correlation: higher concrete strength correlates with a lower strength enhancement ratio, and vice versa. For example, specimen A17 (50 MPa) has a strength enhancement ratio about 50 % greater than A1 (72.4 MPa) at an aspect ratio of 1.0 (Fig. 9A). This effect is less pronounced at an aspect ratio of 1.3, where A18's ratio is 38 % higher than A2 (Fig. 9B). This trend continues for aspect ratios of 1.7 and 2.0. As aspect ratios increase, the strength enhancement ratio decreases due to reduced uniformity of FRP confining pressure. A similar trend is observed in the strain enhancement ratio, with A17's ratio being 47 % greater than A1's at an aspect ratio of 1.0 (Fig. 9).

Moreover, as it is depicted in Fig. 9(c), the strain enhancement ratio of the A19 specimen is 85 % higher than that of the A3 specimen when the aspect ratio is 1.7. By comparing Figs. 10A and 10D, it is feasible to determine that the influence of the strain enhancement ratio is less significant when the aspect ratio is increased from 1.0 to 2.0.

Fig. 10 (E, F) shows the relationship between concrete strength and the strength enhancement ratio for specimens D1-D8 and D13-D16, with concrete strengths of 41.2, 53.6, and 75.7 MPa (Liu et al. [42]). The data indicates that an increase in aspect ratio leads to a decrease in the strength enhancement ratio. For example, specimen D1 (41.2 MPa) has a strength enhancement ratio 66 % greater than D13 (75.7 MPa) at an aspect ratio of 1.0 and FRP thickness of 2.89 mm.

The impact of concrete strength on the strength enhancement ratio is shown in Fig. 11 (A, B), using two different FRP thicknesses: 0.171 mm (one layer) and 0.342 mm (two layers). The data includes experimental specimens from Teng et al. [12] and simulated models. When the FRP thickness is increased from 0.171 mm (one layer) to 0.342 mm (two layers), there is an increase in the strength enhancement ratio, as shown in Fig. 15B. From Teng et al. [12], the impact of concrete strength on the strain enhancement ratio for both one layer of FRP (0.171 mm) and two layers of FRP (0.342 mm) is reported in Fig. 11(A, B). Fig. 11(C, D) shows no direct relationship between the strain enhancement ratio and concrete strength for a single layer of FRP wrap. However, for two layers of FRP wrap, there is no relationship between the strain enhancement ratio and the increase in concrete strength, as reported in Fig. 11(C, D).

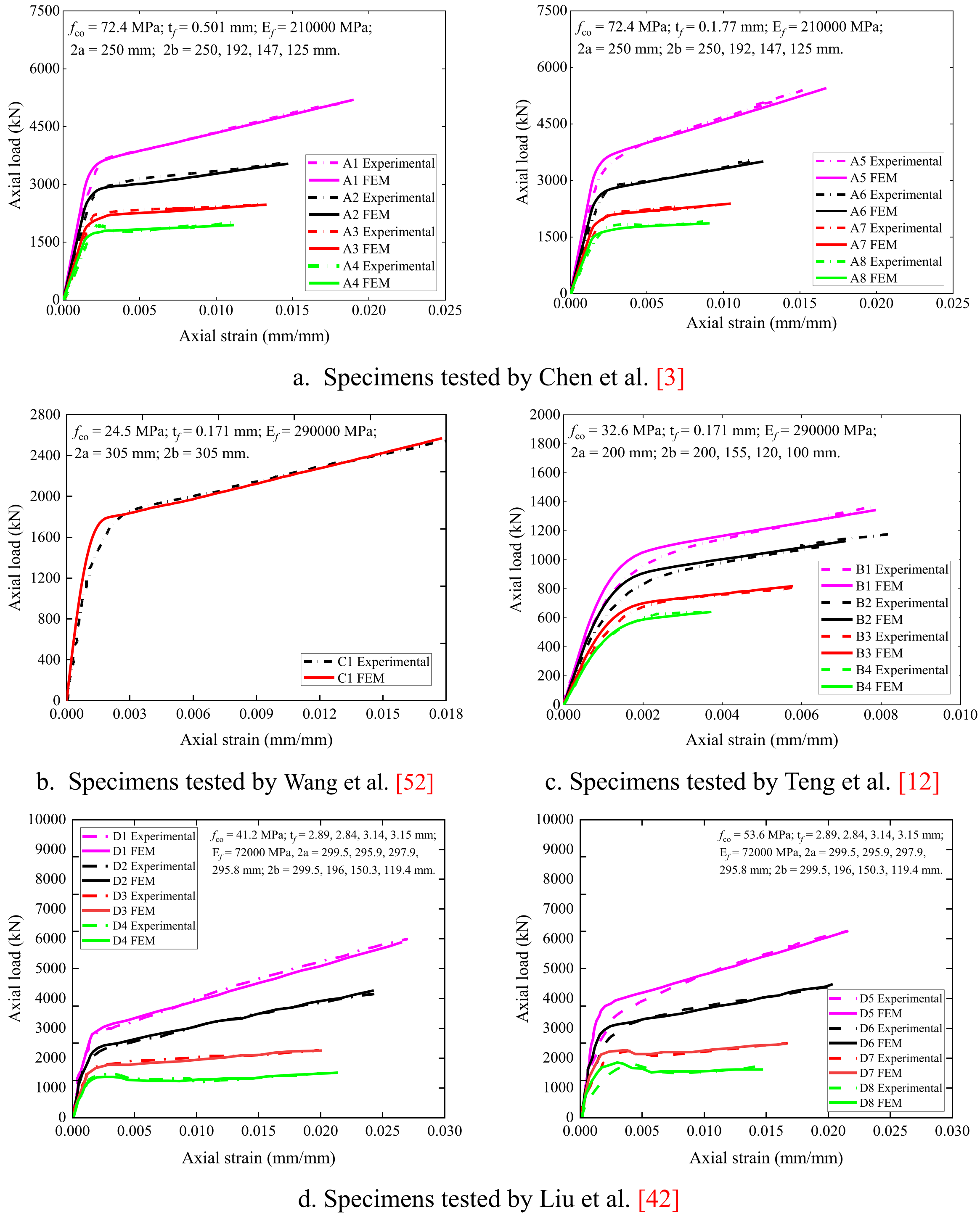

Fig. 6. Comparison between experimental and FEM results from Chen et al. [3], Wang et al. [52], Teng et al. [12], and Liu et al. [42].

5.3.2. *Effect of variation in the number of FRP layers*

The impact of changing the number of layers of CFRP and GFRP on the strain enhancement ratio is shown in Fig. 12. The data includes experimental results from Chen et al. [3] and numerical data from a parametric study. In general, GFRP layers show a better strain enhancement ratio compared to CFRP layers. According to Chen et al. [3], increasing the level of confinement could offset any decrease in effectiveness due to the opposing effects of the increasing sectional aspect ratio.

Fig. 13 depicts the influence of the number of CFRP/GFRP jackets on the strength enhancement ratio, utilizing both experimental results from Chen et al. [3] and numerical data from a parametric study. Conversely, as compared to Fig. 12, Fig. 13A reveals that the strength enhancement ratio does not increase significantly as the number of CFRP layers increases. With the increase in the aspect ratio, the rate of strength enhancement ratio is slow, whereas, for the lower aspect ratio, the rate of strength enhancement ratio is more observed for CFRP layers. In contrast to CFRP, GFRP layers exhibit a higher strength enhancement ratio at aspect ratios of 1.0 and 1.3, respectively. With the increase in the aspect ratio to 2.0, the rate of strength enhancement ratio is lower, as shown in Fig. 13B.

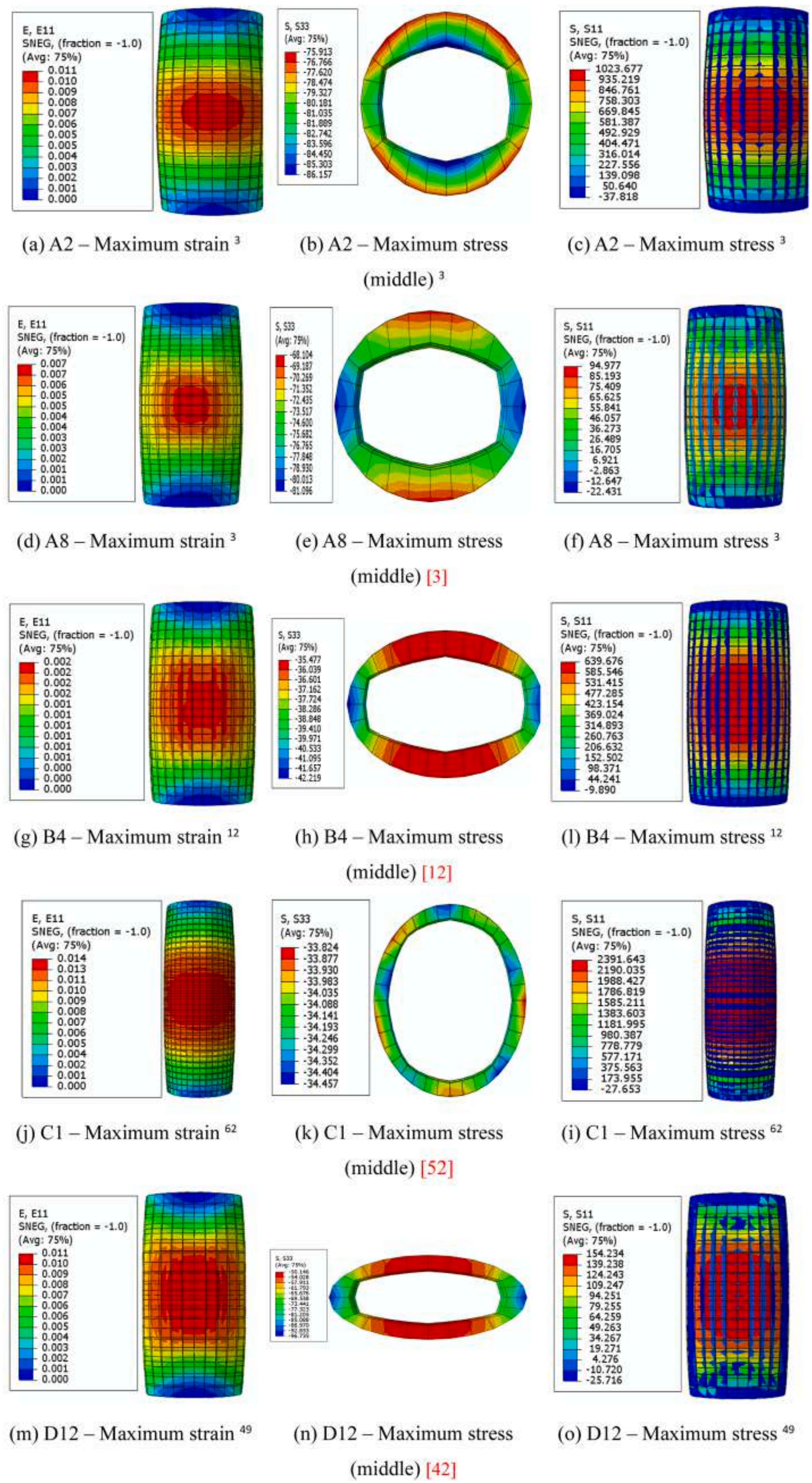

(a) A2 – Maximum strain [3]
(b) A2 – Maximum stress (middle) [3]
(c) A2 – Maximum stress [3]

(d) A8 – Maximum strain [3]
(e) A8 – Maximum stress (middle) [3]
(f) A8 – Maximum stress [3]

(g) B4 – Maximum strain [12]
(h) B4 – Maximum stress (middle) [12]
(l) B4 – Maximum stress [12]

(j) C1 – Maximum strain [62]
(k) C1 – Maximum stress (middle) [52]
(i) C1 – Maximum stress [62]

(m) D12 – Maximum strain [49]
(n) D12 – Maximum stress (middle) [42]
(o) D12 – Maximum stress [49]

Fig. 7. Stress and strain behavior for simulated specimens.

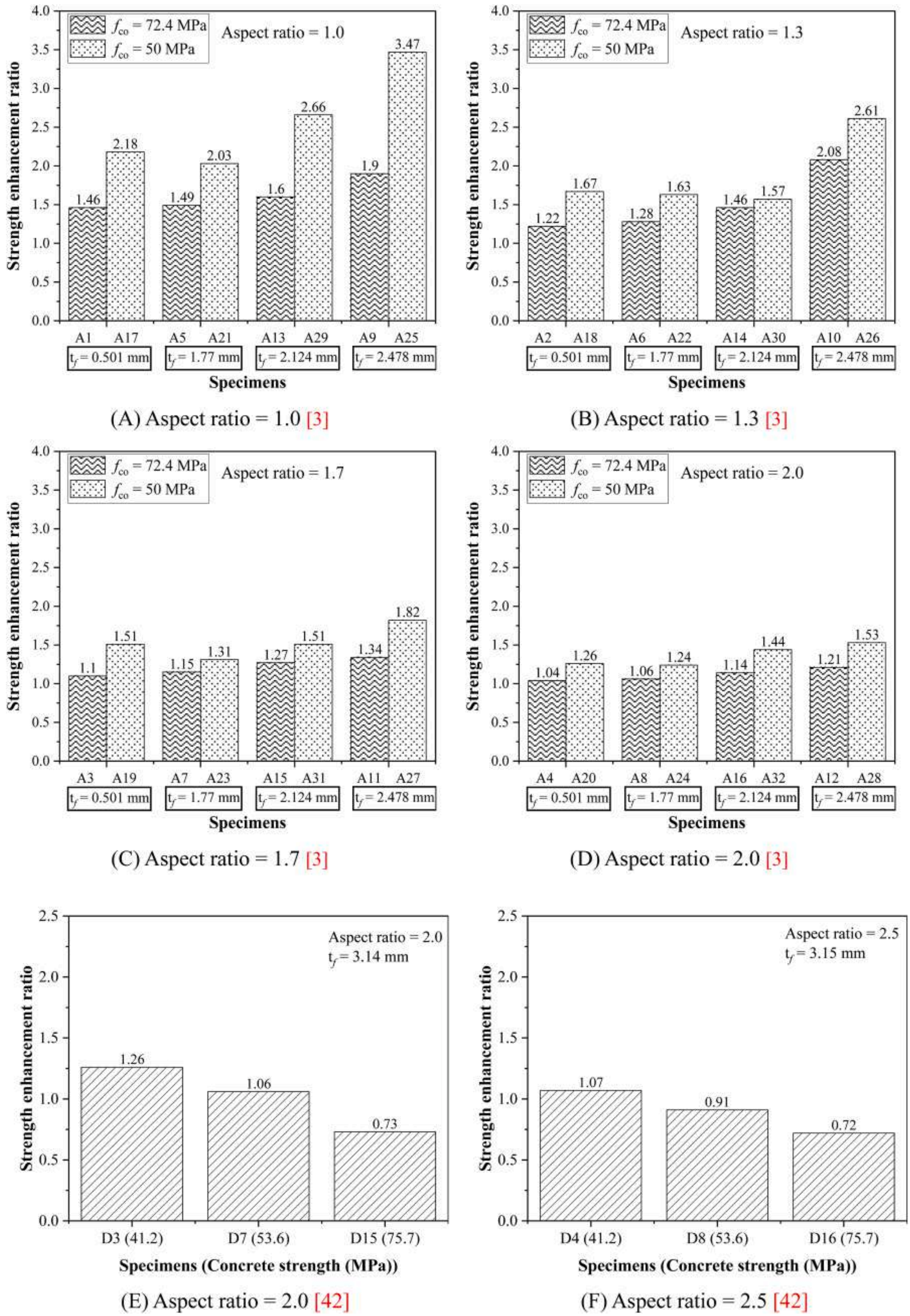

Fig. 8. Impact of concrete strength on strength enhancement ratio for experimental specimens taken from Chen et al. [3] and Liu et al. [42] and simulated specimens.

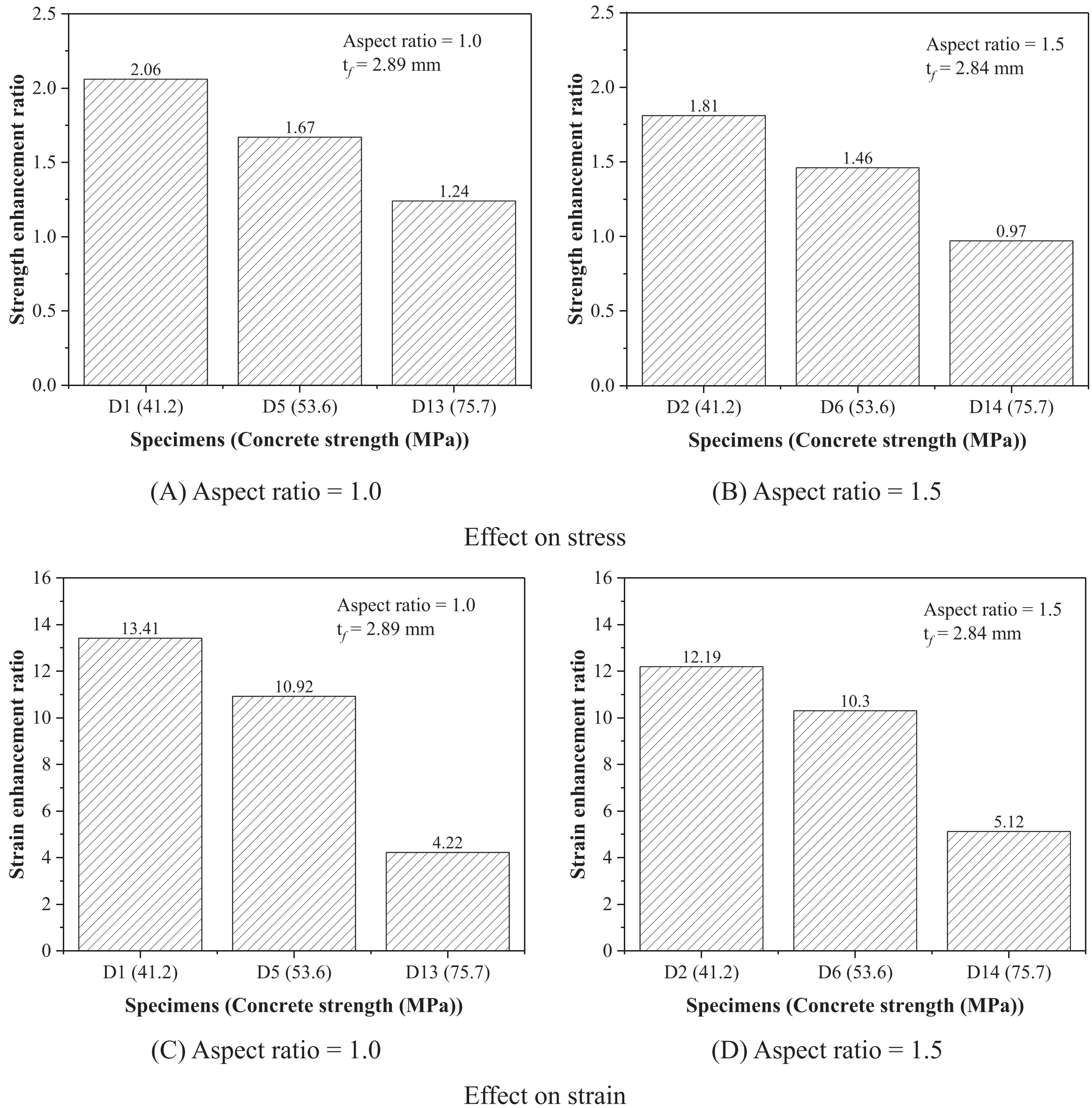

Fig. 9. Impact of concrete strength on strength and strain enhancement ratio for experimental specimens taken from Liu et al. [42].

5.3.3. *Effect of variation in sectional aspect ratio*

It is clear from Fig. 14, for different aspect ratios and thickness of FRP layers, that the axial load and axial strain is decreasing with increasing the sectional aspect ratio. Increasing the number of FRP layers for the same aspect ratio leads to an increase in the axial load and axial strain capacities.

Fig. 15 demonstrates the influence of the aspect ratio on the axial load and axial strain capacities using both simulated results from a thorough parametric study and experimental results from Teng et al. [12]. Similar to the observations in Fig. 14, a descending pattern can be seen in the axial load and axial strain values with increasing the aspect ratio. Meanwhile, with the increase in the unconfined concrete strength from 32.6 to 46.4 MPa, there is an increase in the axial load and axial strain capacitates for various aspect ratios and single layer of FRP wrap as presented in Figs. 15A and 15B, respectively. As shown in Figs. 15C and 15D, with an increase in the concrete strength from 35.8 to 40.2 MPa and number of FRP layers from one to two, a significant increase in the axial load and strain values can be observed as compared to Figs. 15A and 15B, respectively. A similar behavior is noted for specimens derived from Wang et al. [52] and Liu et al. [42].

6. Machine learning modeling

6.1. *Dataset construction*

Before delving into the application of machine learning models, a comprehensive exploration of the dataset was conducted to gain insights into its characteristics and relationships between variables. Table 3 provides a summary of descriptive statistics for the dataset. This included key metrics such as mean, standard deviation, minimum, maximum, and quartile values for each numerical feature, offering an overview of the central tendency and variability within the data. A pair plot offered a visual representation depicted in Fig. 16 pairwise relationships between different features in the dataset. This exploratory visualization facilitated the identification of potential patterns, trends, and outliers, aiding in the initial assessment of data distribution and correlation. The correlation heatmap, demonstrated in Fig. 17, provides insights into the strength and direction of linear relationships between variables. By visualizing the correlation coefficients, it was possible to identify features that exhibited significant correlations with each other and with the target variable. Upon analysis, it was observed that the

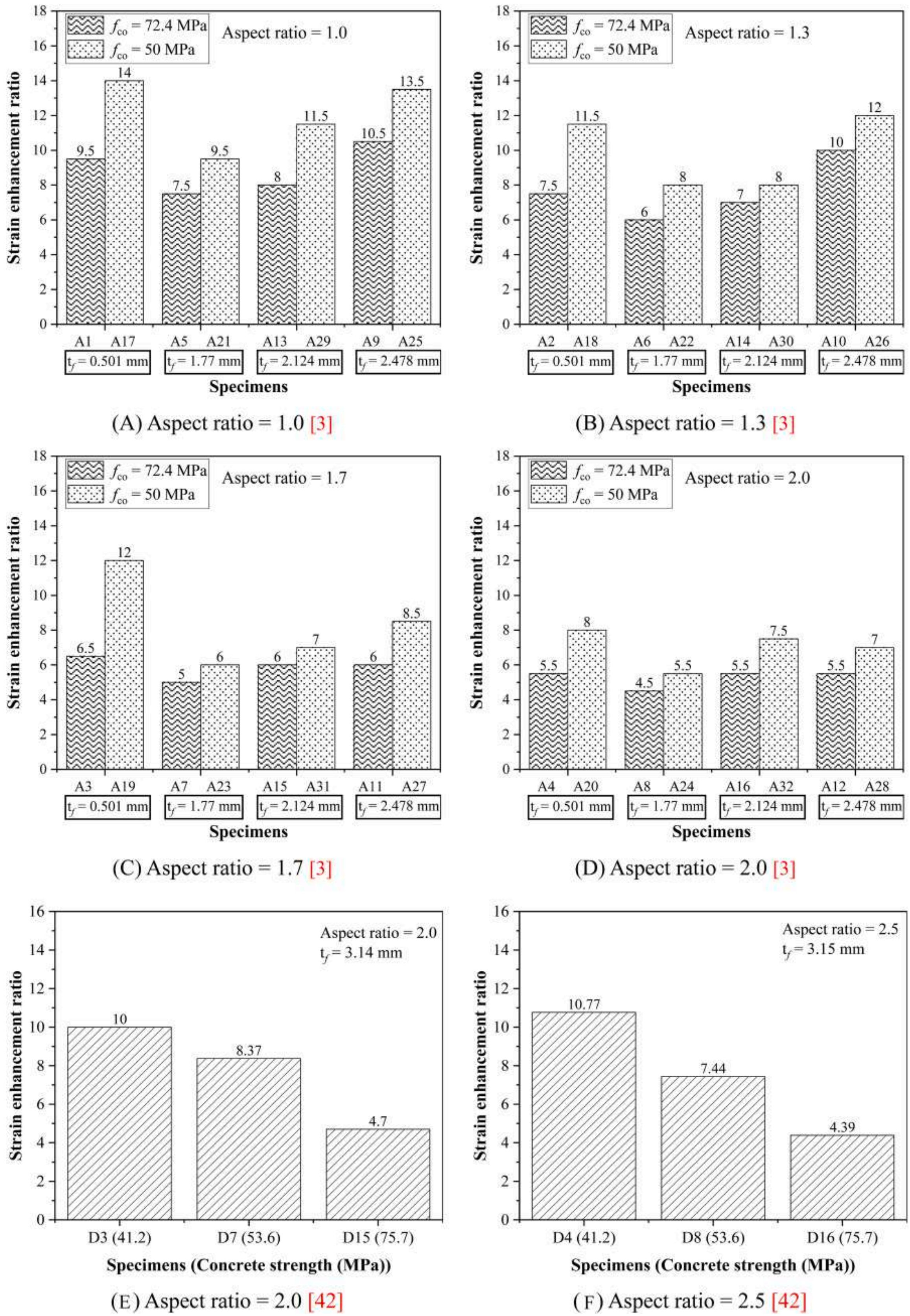

Fig. 10. Impact of concrete strength on strain enhancement ratio for experimental specimens taken from Chen et al. [3] and Liu et al. [42] simulated specimens.

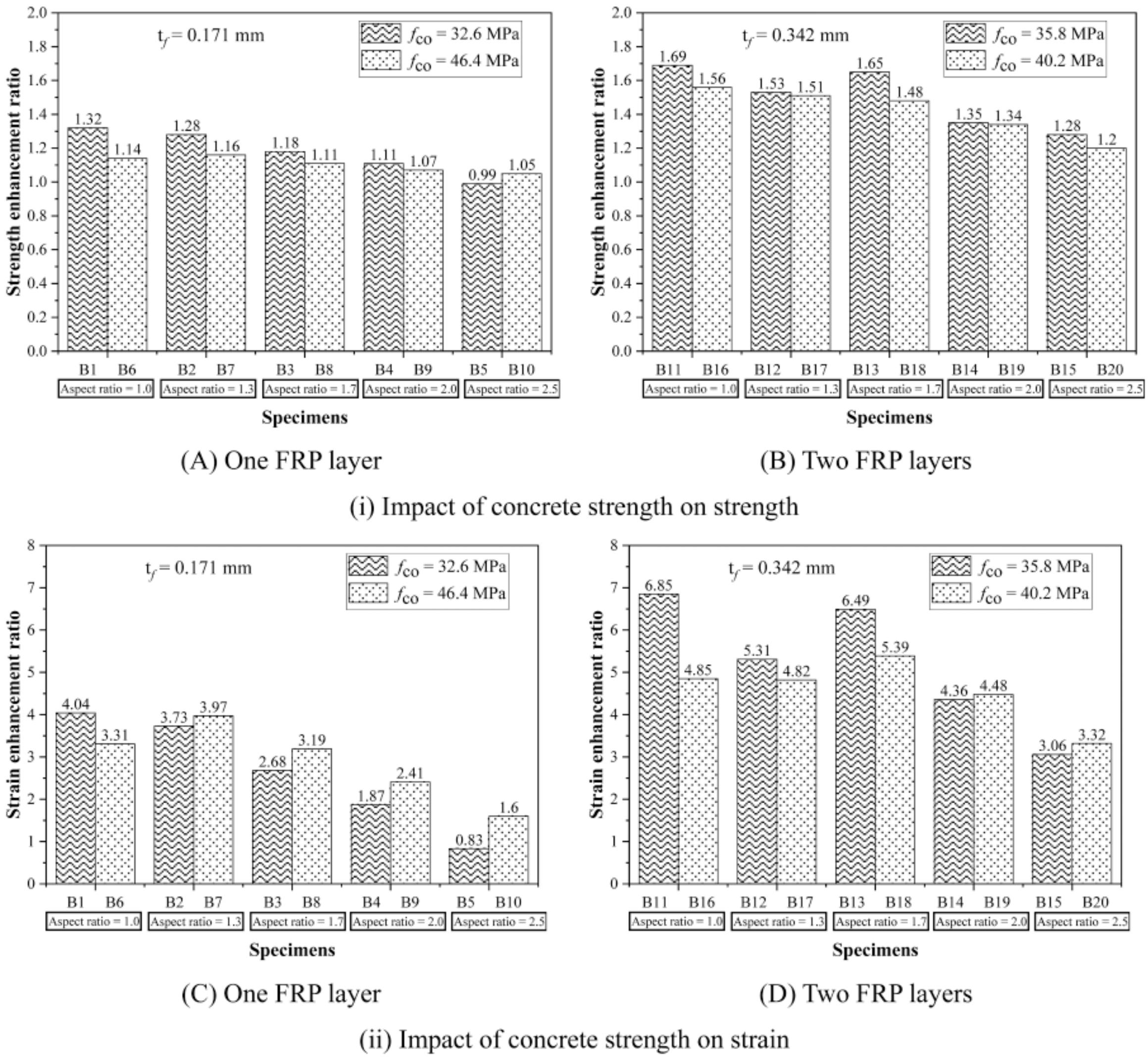

Fig. 11. Impact of concrete strength on strength and strain.

feature named 2*b* (mm), which stands on width of cross section gave the highest correlation with the f_{cc} (MPa) target, indicating a potentially influential role in predicting the target outcome. Conversely, the feature 2*b* (mm), depth stands on depth of cross section displayed the lowest correlation coefficient with the target variable, suggesting a weaker association compared to other features. It should be noticed that the high or low correlation with the target does not guarantee high or low contribution to the model's prediction. In Fig. 18, Histograms were utilized to visualize the distribution of data within each feature, offering insights into the spread and concentration of values.

6.2. Overview of machine learning

Tree-based machine learning models have been pivotal in the predictive tasks, which widely use in engineering problems, offering versatile tools for both classification and regression tasks. These models leverage hierarchical decision structures to partition the feature space and make predictions based on the characteristics of the data. Over time, tree-based algorithms have evolved from simple decision trees to more complex ensemble methods, each with its own distinct advantages and capabilities.

Decision tree model can be considered as foundation of these models, which recursively split the feature space based on the values of input features. The features with lowest Gini Impurity (GI), which calculated using Eq. (4), will be placed at the top nodes of tree [77–79].

$$GI = \sum_{j=1}^{k} \widehat{P}_{i,j}(1 - \widehat{P}_{i,j}) \tag{6}$$

Despite Decision tree's simplicity and interpretability, it suffers from overfitting, particularly when dealing with complex datasets with high-dimensional feature spaces, which currently utilize in engineering. To solve the mentioned drawbacks, Random Forest (RF) model is developed, which multiple decision trees using bootstrapped samples from the dataset and random subsets of features at each node, as shown in Fig. 19.

Another notable advancement in tree-based modeling is Gradient Boosting, which sequentially builds a series of decision trees to correct the errors of the preceding models. Unlike Random Forest, Gradient Boosting focuses on minimizing the residuals of the ensemble by fitting new trees to the negative gradient of the loss function. Through this iterative process, Gradient Boosting gradually improves predictive accuracy and can capture complex relationships within the data.

XGBoost (Extreme Gradient Boosting) represents a further refinement of Gradient Boosting algorithms, introducing enhancements such as regularization techniques and advanced optimization algorithms. XGBoost optimizes a more complex objective function that incorporates regularization terms to prevent overfitting and improve model robustness. Additionally, XGBoost offers efficient distributed computing

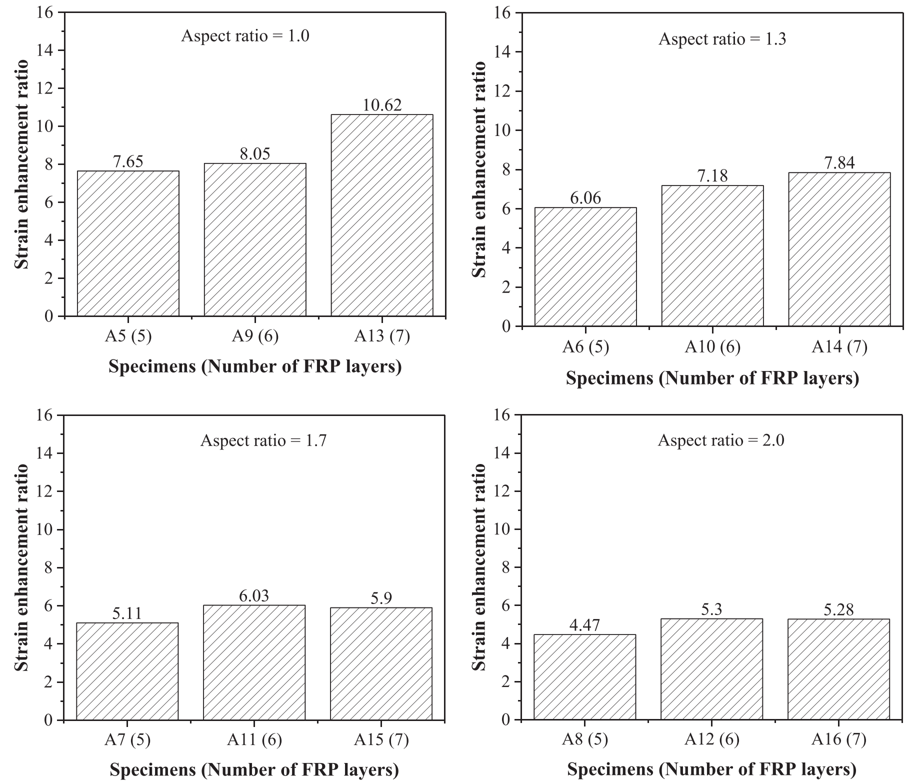

(A) Strain enhancement ratio for specimens with CFRP layers (A5 to A16)

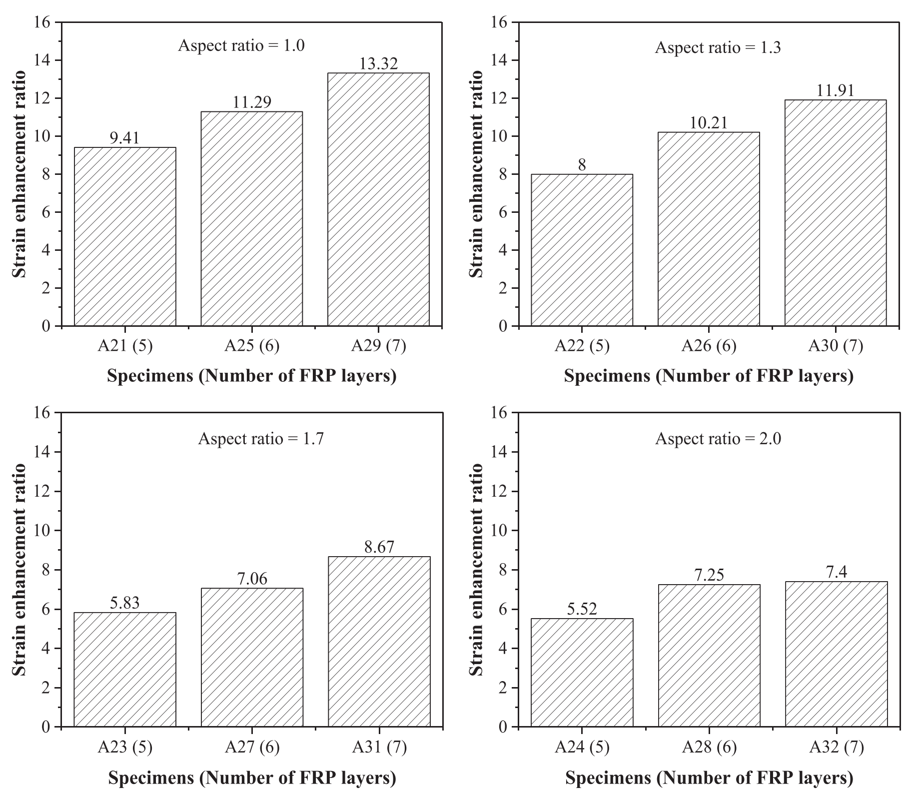

(B) Strain enhancement ratio for specimens with GFRP layers (A21 to A32)

Fig. 12. Impact of the number of FRP layers on the strain.

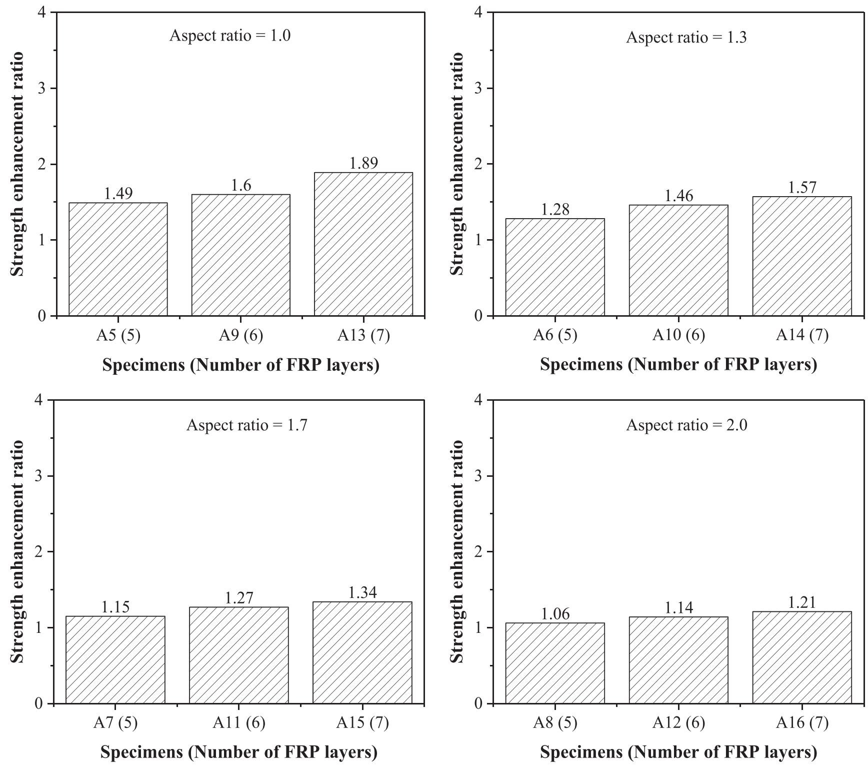

(A) Strength enhancement ratio for specimens with CFRP layers (A5 to A16) [3]

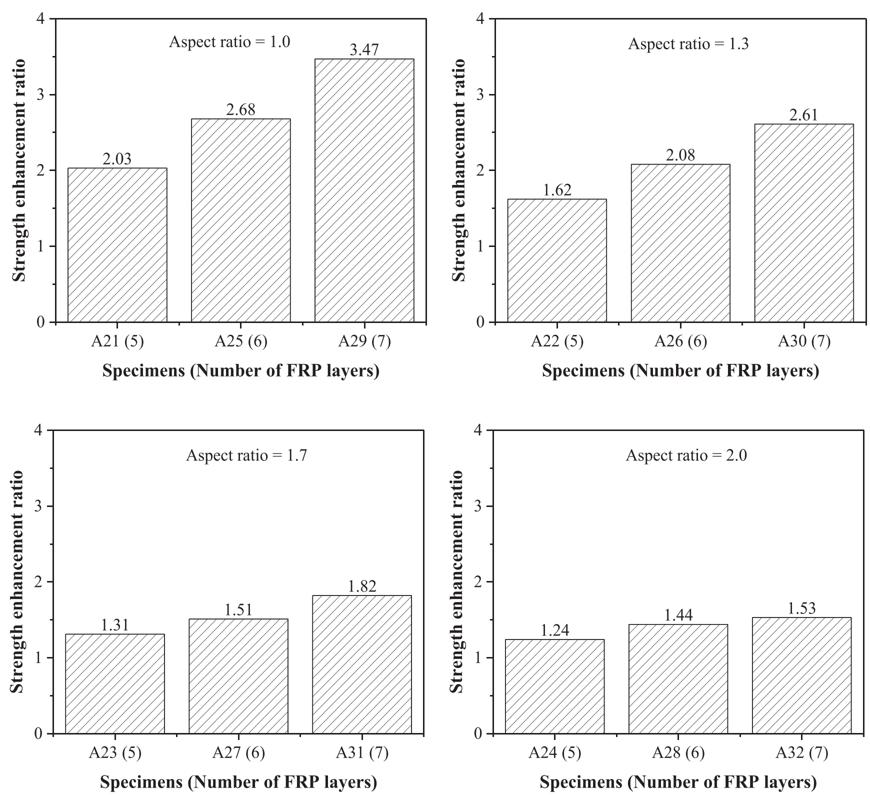

(B) Strength enhancement ratio for specimens with GFRP layers (A21 to A32) [3]

Fig. 13. Impact of the number of FRP layers on strength.

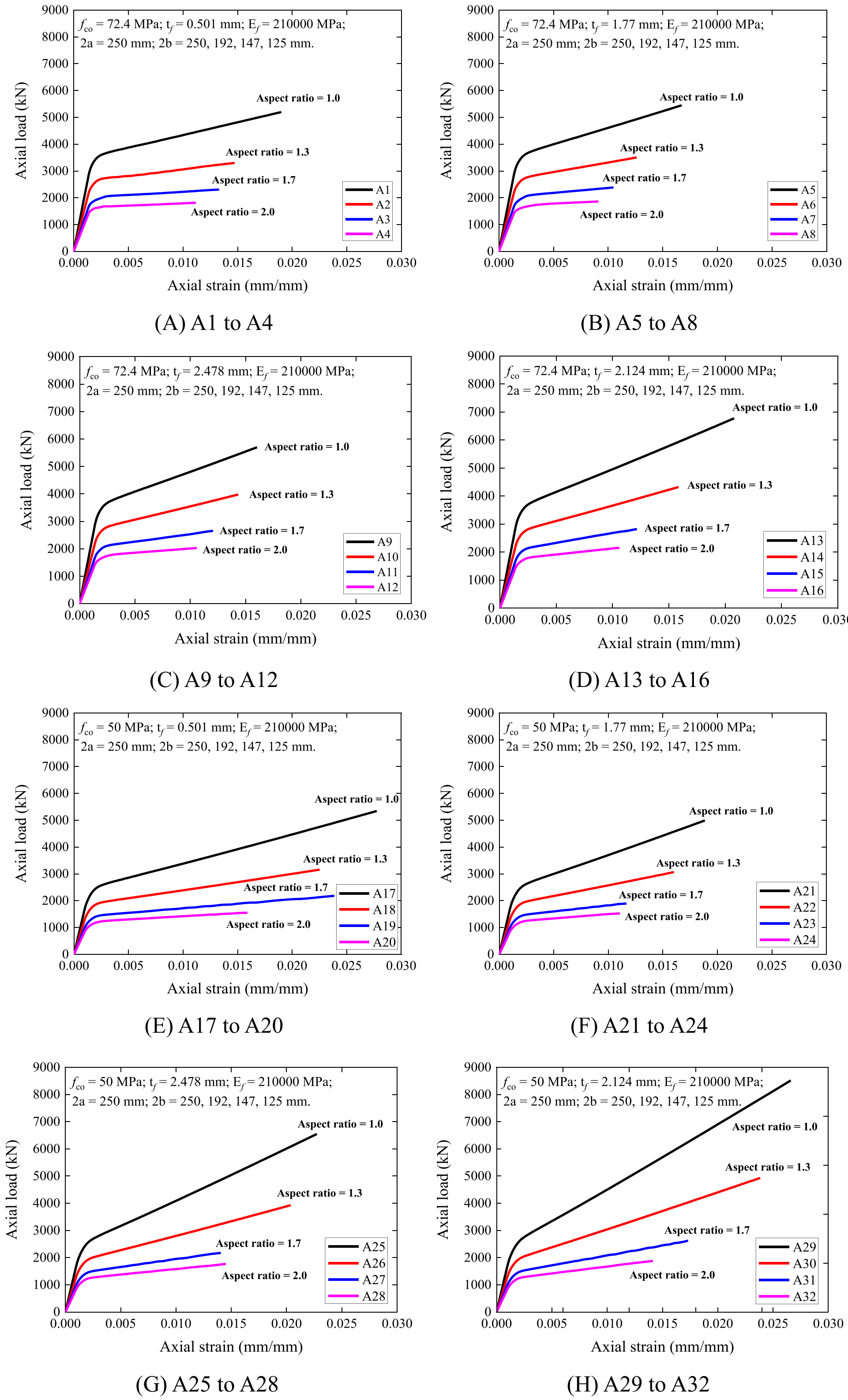

Fig. 14. Effect of sectional aspect ratio on axial load and axial strain relationships for experimental specimens taken from Chen et al. [3] and simulated specimens derived from a parametric study.

capabilities, making it suitable for handling large-scale datasets with millions of samples and features [79].

For evaluating performance of the developed models on prediction, three key metrics were utilized: the coefficient of determination (R^2), the root mean squared error (RMSE), and the mean absolute error (MAE). The R^2 value is a measure of the proportion of the variance in the dependent variable that is predictable from the independent variables, defined in Eq. (5).

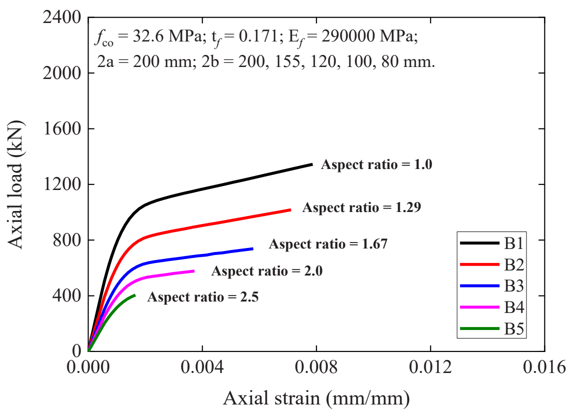

(A) B1 to B5

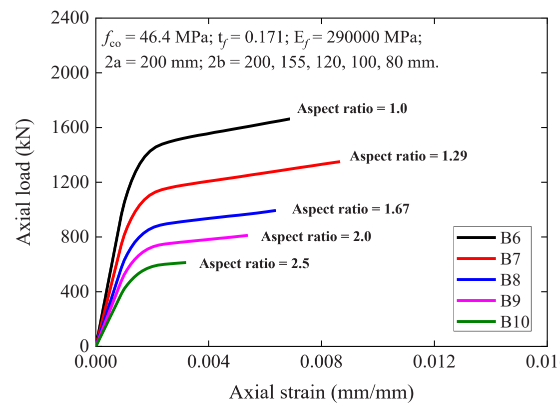

(B) B6 to B10

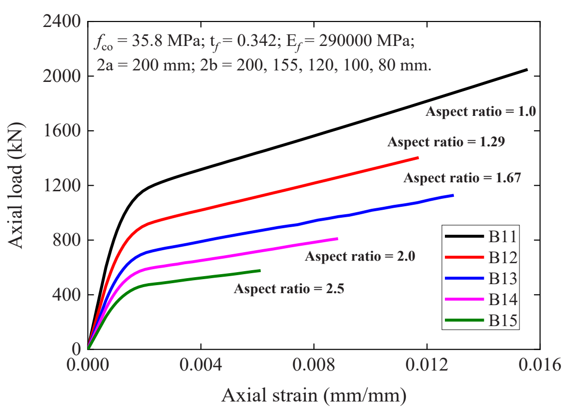

(C) B11 to B15

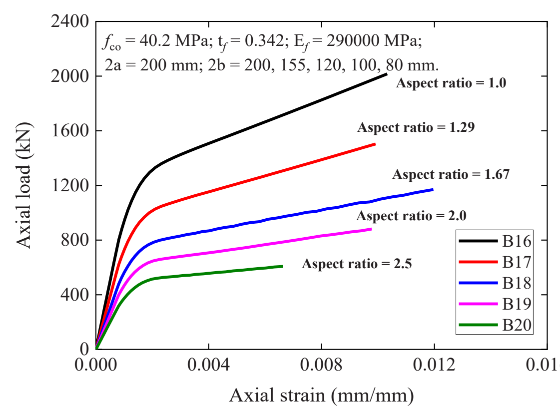

(D) B16 to B19

(I) Teng et al. [12]

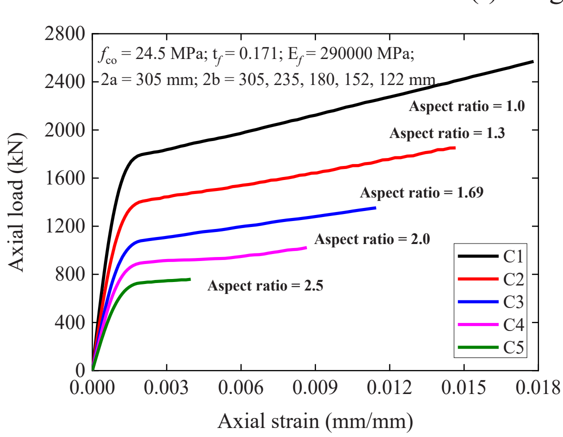

(II) Wang et al. [52]

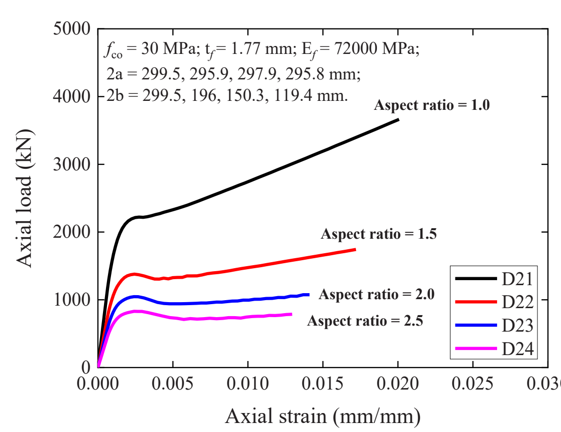

(III) Liu et al. [42]

Fig. 15. Effect of sectional aspect ratio on axial load and axial strain relationships.

Table 3
Statistical properties of dataset.

	f_{co} (MPa)	$t_f \times E_f$ (MPa)	$2a$ (mm)	$2b$ (mm)	f_{cc} (MPa)	ε_{cc} (mm/mm)
Count	130.00	130.00	130.00	130.00	130.00	130.00
Mean	50.17	141,833.35	254.69	173.00	68.63	0.01
Std	16.32	72,652.13	39.74	60.42	28.08	0.01
Min	24.50	49,590.00	200.00	80.00	25.20	0.00
25 %	35.80	99,180.00	200.00	125.00	49.19	0.01
50 %	50.00	127,440.00	250.00	151.15	61.90	0.01
75 %	72.40	178,416.00	295.90	199.00	87.54	0.02
Max	75.70	349,200.00	305.00	305.00	173.40	0.03

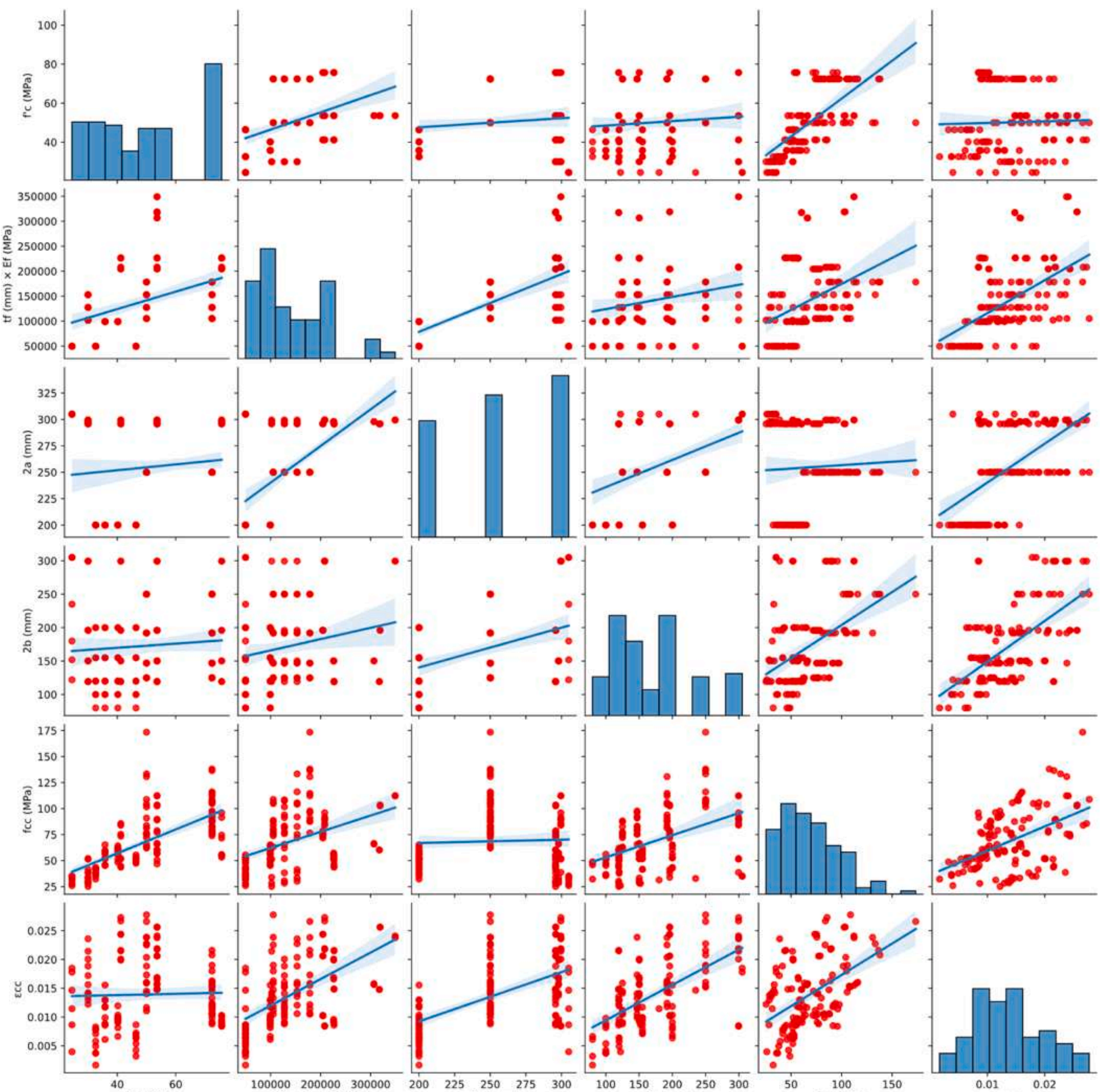

Fig. 16. Scatter plot of dataset.

Fig. 17. Correlation heatmap between output and input variables.

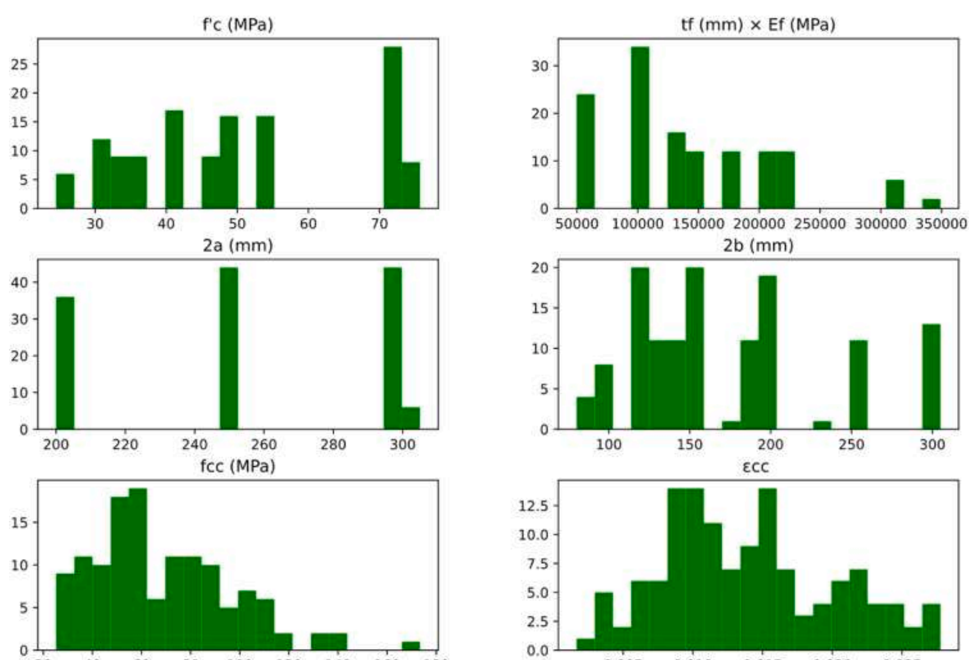

Fig. 18. Histograms of output and input variables.

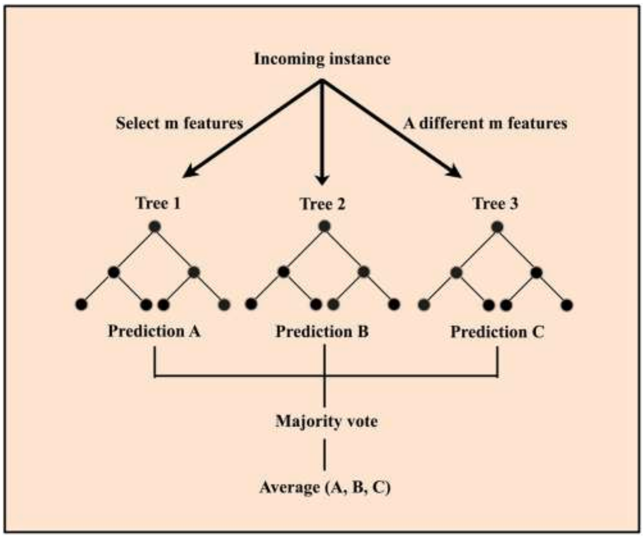

Fig. 19. Schematic of Random Forest model.

$$R^2 = 1 - \frac{SS_{res}}{SS_{tot}} \tag{7}$$

Where SS_{res} is the residual sum of squares and SS_{tot} is the total sum of squares. It quantifies the goodness of fit of the model, with values closer to 1 indicating a better fit. The RMSE and MAE, expressed in Eq. (6), measures the average magnitude of the errors between predicted and actual values, providing insight into the model's accuracy. In Eq. (7), MAE represents the average absolute difference between the predicted and actual values, offering a precise measure of prediction accuracy that is less sensitive to outliers.

$$RMSE = \sqrt{\frac{\sum (\widehat{y}_{test,i} - y_{test,i})^2}{N}} \tag{8}$$

$$MAE = \frac{1}{n}\sum_{i=1}^{n} |y_i - \widehat{y}_i| \tag{9}$$

6.3. Hyperparameters tuning using Randomized Search CV

Machine learning algorithms often have hyperparameters, which are settings that control the learning process but are not learned from the data. For assessing to best performance of ML models, it is crucial to tune their hyperparameters. Grid search method can be considered as an effective way for hyperparameters tuning. As illustrated in Fig. 20, this method systematically searches through a specified grid of hyperparameters for a model and return the best values of hyperparameters. The desired hyperparameters and their possible ranges and values for hyperparameter tuning, using grid search, are listed in Tables 4 to 6.

Table 4
DT grid search parameters.

Max depth	Min samples leaf	Min samples split	Max features
None	1	2	'auto'
3	2	5	'sqrt'
5	4	10	'log2'
7	8	20	None
10	-	-	-

Table 5
RF grid search parameters.

N estimators	Max depth	Min samples leaf	Min samples split	Max features
50	None	1	2	'auto'
100	10	2	5	'sqrt'
200	20	4	10	'log2'
300	30	8	20	None

Table 6
GB and XGB grid search parameters.

Learning rate	N estimators	Max depth
0.01	50	3
0.1	100	5
0.2	200	7
0.3	300	9
0.5		12

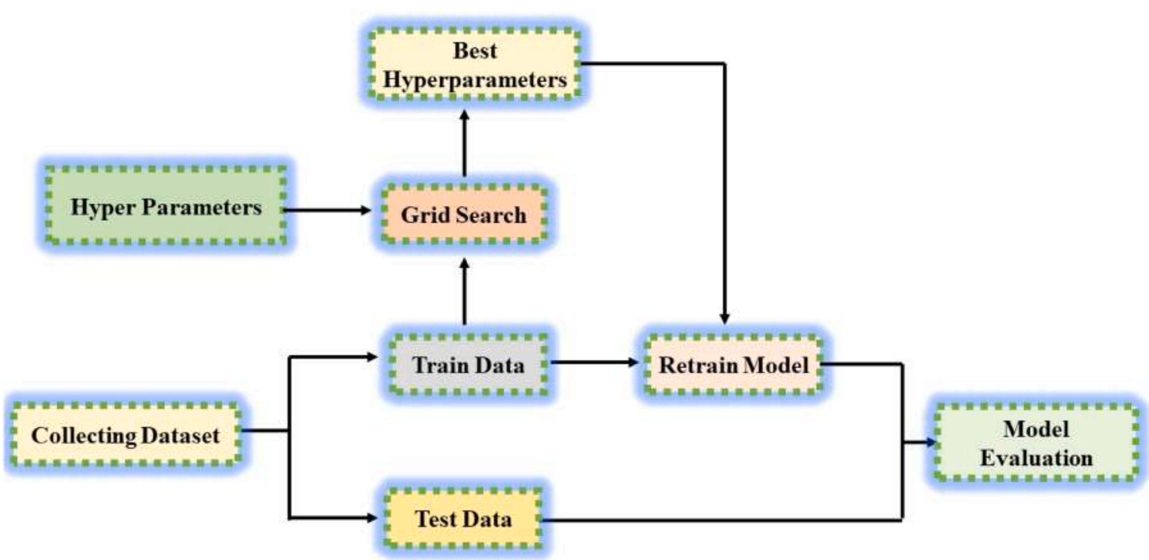

Fig. 20. Grid search method flowchart.

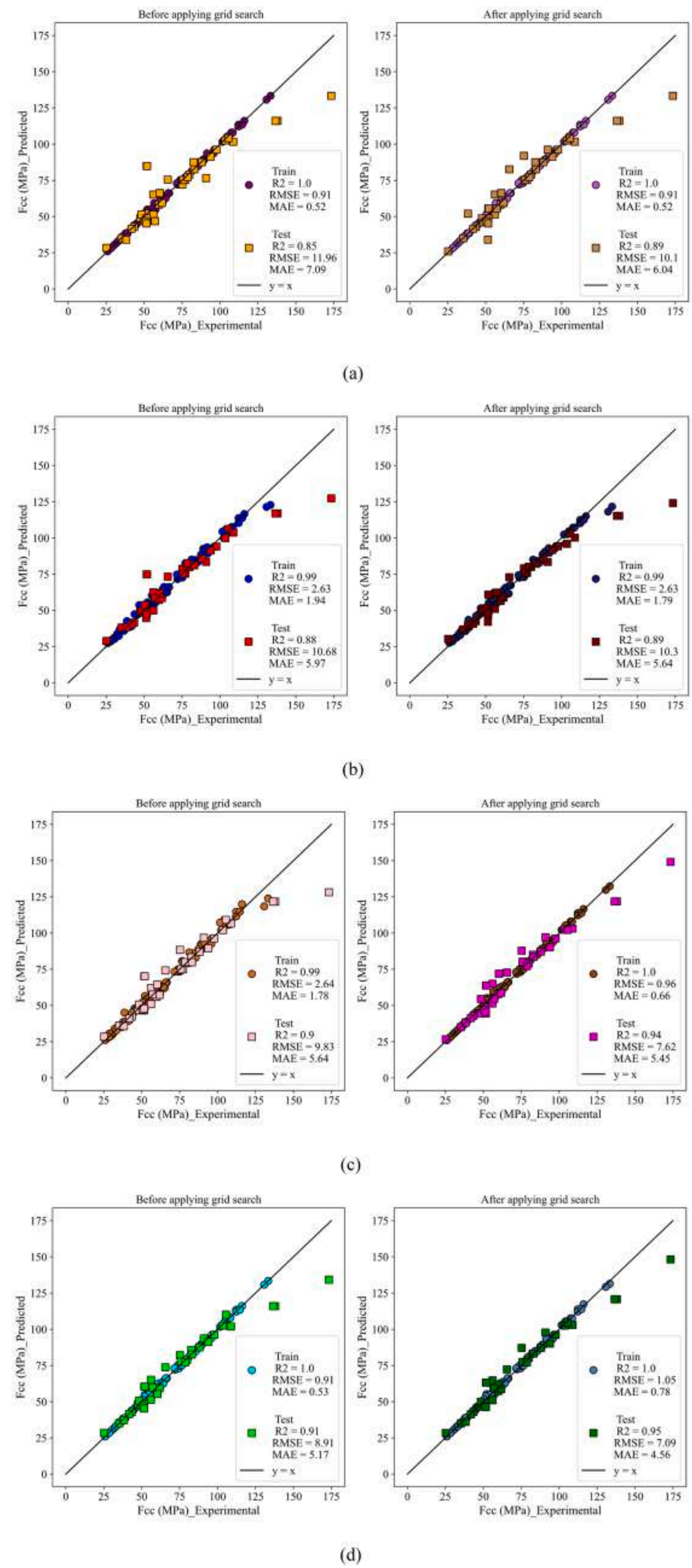

Fig. 21. ML models result with the target of f_{cc} (MPa): (a) DT, (b) RF, (c) GB, and (d) XGB.

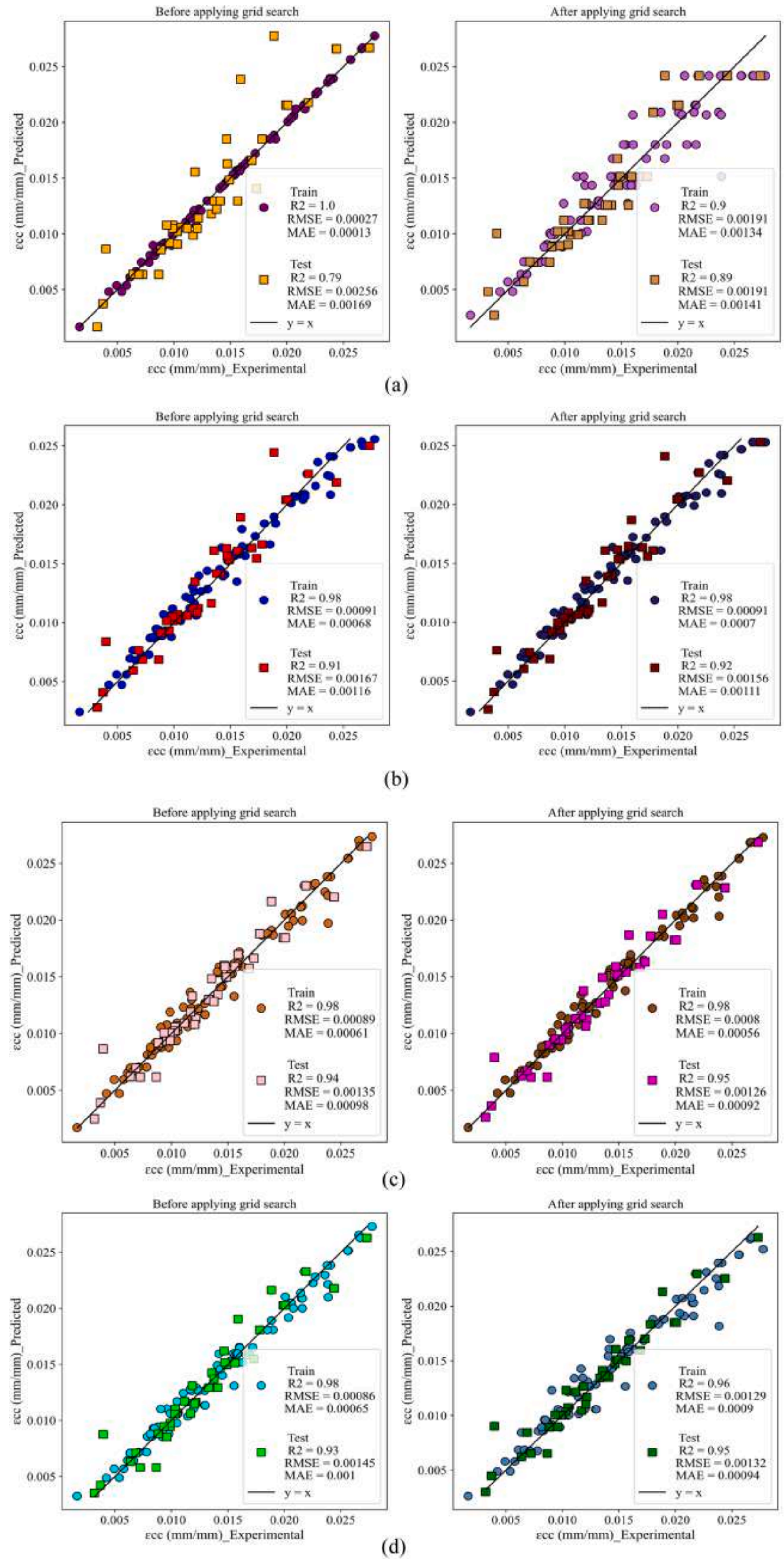

Fig. 22. ML models results with the target of ε_{cc} (mm/mm): (a) DT, (b) RF, (c) GB, and (d) XGB.

Table 7
Best hyperparameters resulting from grid search: f_{cc} (MPa).

Model	N estimators	Max depth	Learning rate	Min sample leaf	Min sample split	Max features	Random state
DT	-	10	-	1	2	sqrt	0
RF	200	None	-	1	2	sqrt	0
GB	200	3	0.5	-	-	-	0
XGB	300	3	0.3	-	-	-	0
Train_Test_split	0						

Table 8
Best hyperparameters resulting from grid search: ε_{cc} (mm/mm).

Model	N estimators	Max depth	Learning rate	Min sample leaf	Min sample split	Max features	Random state
DT	-	5	-	2	2	auto	0
RF	50	None	-	1	2	auto	0
GB	50	3	0.2	-	-	-	0
XGB	100	3	0.1	-	-	-	0
Train_Test_split	10						

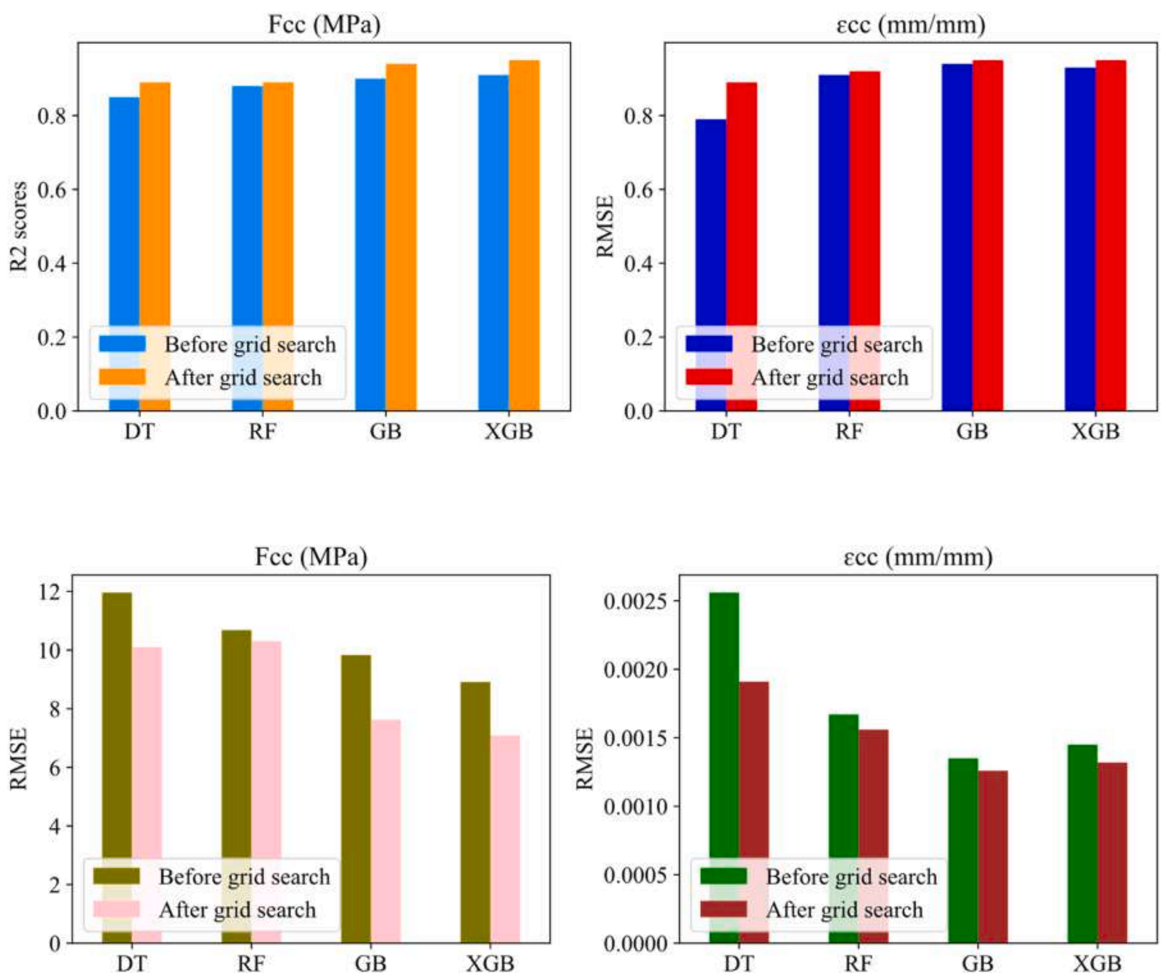

Fig. 23. Impact of grid search on ML models' results.

7. Machine learning results

In this study, four tree-based ML models, including DT, RF, GB, XGB were implemented. The result of mentioned models with the target of f_{cc} (MPa) and ε_{cc} (mm/mm) are indicated in Figs. 21 and 22, before and after applying grid search for hyperparameters, respectively. It can be seen as a mild growth in the scores of the ML models' results, which obviously exhibits the efficiency of grid search. Among the models with

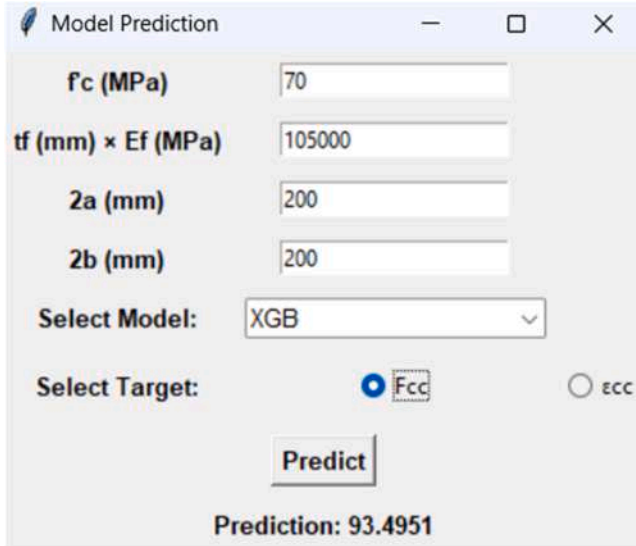

Fig. 24. GUI of ML models.

the target of ε_{cc} (mm/mm), XGB and GB models achieve the highest score, accounting for 0.95. Additionally, the XGB model with a score of 0.95 is assumed to be the best model for the target of f_{cc} (MPa).

The best values for most important hyperparameters, which resulted from grid search are shown in Tables 7 and 8 with both targets, f_{cc} (MPa) and ε_{cc} (mm/mm). Moreover, the impact of hyperparameters tuning, implemented by grid search can be observed in Fig. 23.

To make it easier for users to access and utilize these ML models, the GUI of the models is designed as illustrated in Fig. 24. Additionally, the open-source code for the GUI is available on GitHub.

7.1. Features importance

In order to interpreting the black box of ML models, SHapley value are used in this study. SHapley values, originating from cooperative game theory, offer a powerful framework for interpreting the contributions of individual features within machine learning models [80] (Fig. 25). As Eq. (8) demonstrates, the Shapley value $\varnothing_i$ for feature i is calculated as the average marginal contribution of that feature across all possible permutations of features, where N is the set of all features, S designates a subset of features excluding feature i, $|S|$ denotes the cardinality of set S, $v(S)$ is the model's prediction when only features in set S are considered, and $v(S\cup\{i\})$ is the model's prediction when feature i is added to set S [81,82].

$$\phi_i = \sum_{S\subsetneq N\{i\}} \frac{|s|!(|N|-|S|-1)!}{|N|!}[v(S\cup\{i\})-v(S)] \tag{10}$$

The SHapley values for each record on test data separately are presented in Fig. 26, while Fig. 27 indicates the mean SHapley values of each feature on the model's prediction on test data. Also, the rank of each feature's importance is visible in both Fig. 26 and Fig. 27. As a general trend, it can be seen that $2a$ (mm) and $t_f(mm)\times E_f(MPa)$ achieved the last rank in the feature importance of the XGBoost model with the target f_{cc} (MPa) and the target ε_{cc} (mm) respectively. The f_{co} feature can be considered as most important feature in both models.

7.1.1. Genetic expression programming proposed model

In an effort to propose an explicit formula to calculate Confined concrete strength, genetic expression programming (GEP) is used. In GEP, chromosomes are constructed with linear sequences containing genes representing features, targets, or operators. Each gene consists of a head and a tail section, where operators are not allowed in the tail section. The length of the head section is defined by user, while the tail section's length depends on the maximum number of operator arguments and the head length. After constructing chromosomes, their fitness is determined by expressing them as expression trees (ETs) and evaluating their predicted values against real targets in a given dataset [77,83]. This process helps measure the accuracy of the chromosome's

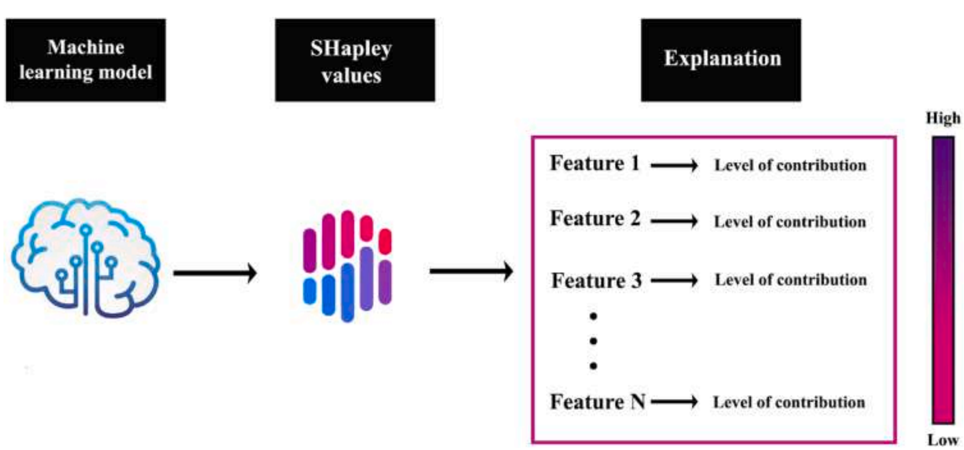

Fig. 25. Workflow of Shapley values method.

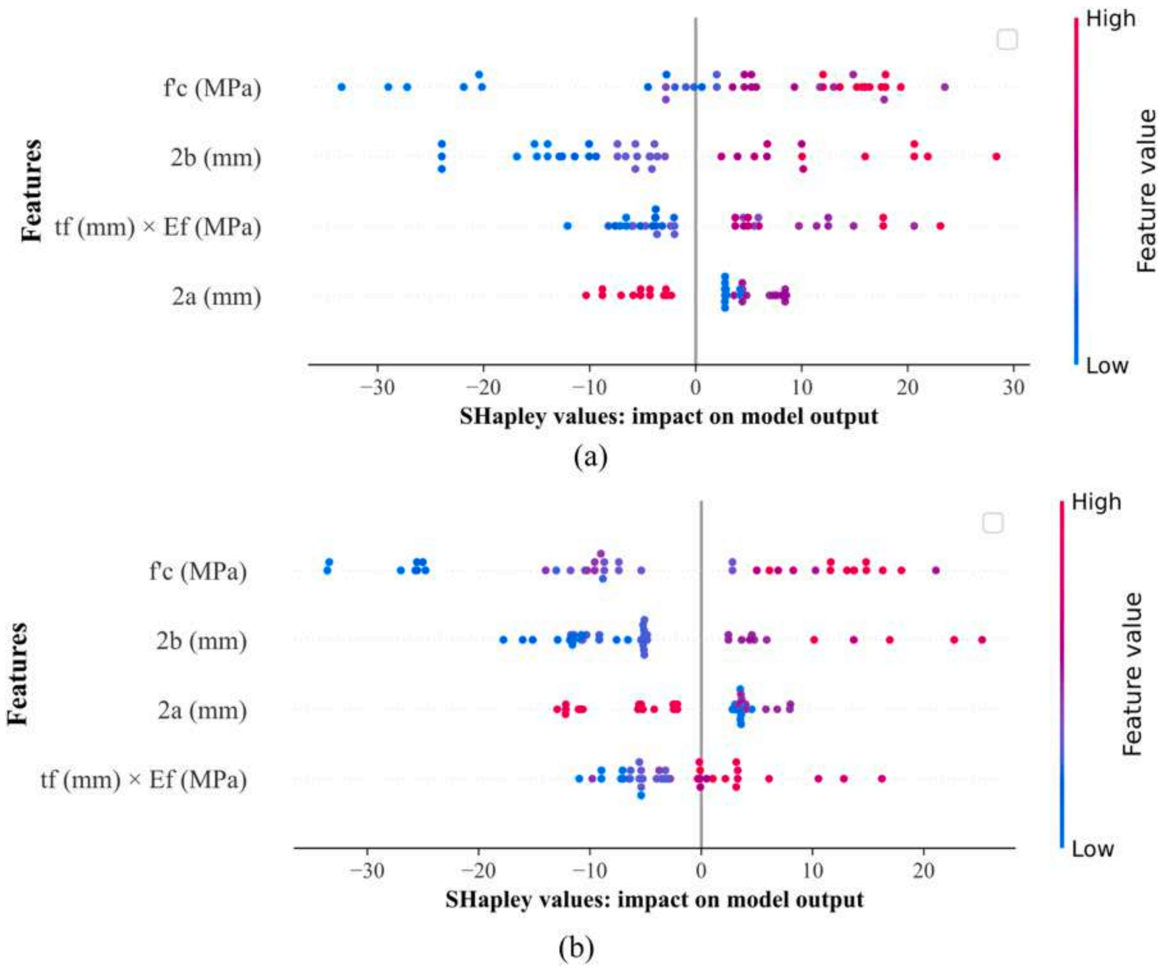

Fig. 26. SHapley values of XGB model: (a) with the target of f_{cc} (MPa), (b) with the target of ε_{cc} (mm/mm).

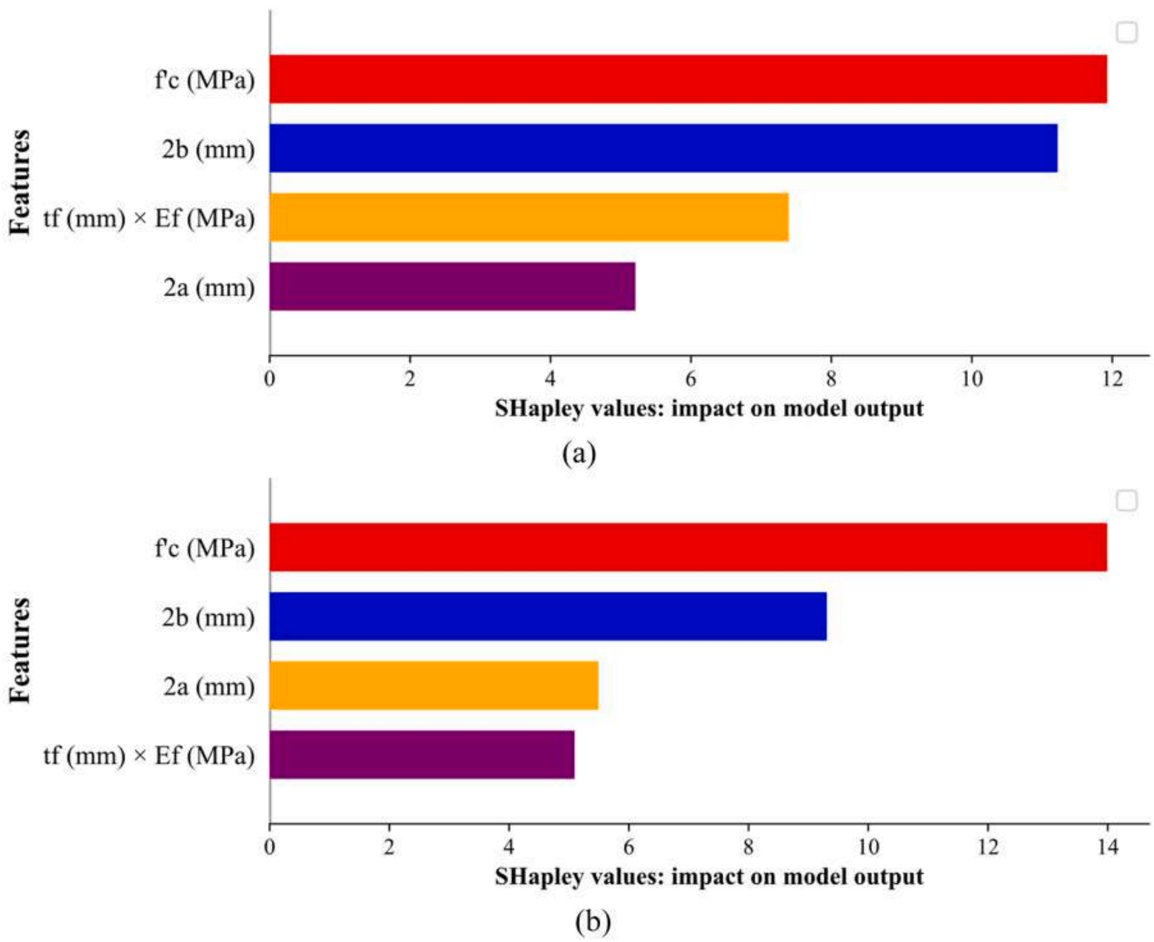

Fig. 27. Mean SHapley values of each feature of XGB model: (a) with the target of f_{cc} (MPa), (b) with the target of ε_{cc} (mm/mm).

predictions. Based on this method, a formula presented in Eq. (9) and Fig. 28 for calculating confined concrete strength is proposed and the parameters, which used in this model are outlined in Table 9. It should be noted that the inputs should be normalized using standard scaler (Eq. (10)). The result of proposed formula in this dataset are given in Fig. 29.

$$F_{GEP} = F_1 + F_2 + F_3 \tag{11}$$

$$F_1 = Arctan(\max(d_0, (d_1 - m)))$$

$$m = d_1 - \min(d_0 - 1.19) - \left(\frac{d_2 + d_3}{2}\right)$$

$$F_2 = sin(\max(d_3, k) - 0.18\ )$$

$$k = Arctan(\min(-0.89 - d_1), d_0)$$

$$F_3 = \tanh(d_2(\max(d_1, d_2)\ ) * (d_3 - 6.65) * \exp(d_3))$$

$$F_{final} = \frac{F_{GEP} - F_{ave}}{F_{std}} * Target_{stdev} + Target_{ave}$$

$$F_{ave} = 0.00253 \quad , \quad F_{std} = 0.93$$

$$Target_{ave} = 68.46 \quad , \quad Target_{stdev} = 28.85$$

$$Z = \frac{x_i - x_{mean}}{x_{std}} \tag{12}$$

$$d_0 : f_{co} \quad (MPa) : \quad x_{mean} = 49.5, \quad x_{std} = 16.29$$

$$d_1 : t_{\ f}(mm) * E_{\ f} \quad (MPa) : \quad x_{mean} = 140964.4, \quad x_{std} = 71691.91$$

$$d_2 : 2a \quad (mm) : \quad x_{mean} = 256.09, \quad x_{std} = 40.62$$

$$d_3 : 2b \quad (mm) : \quad x_{mean} = 177.74, \quad x_{std} = 61.42$$

8. Conclusions

The current study investigates 85 elliptical concrete columns wrapped with FRP (CFRP and GFRP) jacket subjected to axial compressive strength. The FE modeling was developed and validated with the experimental data mentioned earlier. Regression analysis is performed to establish the model, and ML techniques validate it. The following conclusions can most properly be drawn:

- The ultimate axial stress and corresponding axial strain increase with more FRP layers, but non-uniform FRP distribution negatively affects the axial behavior of elliptical FRP-confined concrete columns. High-strength concrete is stiffer and experiences less cracking, resulting in a longer delay between axial strain and confining stress.
- For different aspect ratios and thicknesses of FRP layers, it was observed that the axial load and axial strain decrease with increasing sectional aspect ratio. Additionally, increasing the number of FRP layers for the same aspect ratio leads to an increase in the axial load and axial strain capacities.
- Comparing GFRP to CFRP layers, the former often exhibit a greater ratio of enhanced strain. This suggests that GFRP layers have a generally higher capacity to increase deformation under stress than CFRP layers. The unique qualities of the materials, their interactions with the matrix, or the production techniques used could all be contributing factors to this superiority.
- In general, the FEM technique provided a good prediction of the axial performance of elliptical CFRP/GFRP-confined concrete columns.
- With the R^2 values of 0.95, XGB outperformed the other four tree-based machine learning models in terms of predictive accuracy for both the f_{cc} and ε_{cc} targets.
- Grid search hyperparameter tuning produced better results for all models, indicating its significance in optimizing ML model capabilities.
- The f_{co} feature was found to have the greatest influence on SHapley value analysis for predicting confined concrete strength across targets, whereas the 2a parameter had the least effect.
- Using the raw input features, the proposed GEP formula offers a clear and simple method for directly determining the strength of elliptical concrete columns.

To provide a more comprehensive understanding of the research context and to acknowledge potential constraints or challenges in the findings, it is essential to list out the limitations of the current study. Some limitations include:

- The study uses the assumption that FRP materials have uniform characteristics; it ignores possible differences in manufacture or use that can affect how successful these materials are at confining concrete.
- The axial compressive behavior under static loading situations is the main emphasis of the model. It might not be as reliable in forecasting dynamic responses or other loading modes, including lateral loads.
- Although the article's primary focus is on elliptical cross-sections, it may not fully depict the range of geometric changes found in real-world buildings.
- Numerous studies, including this one, simplify by assuming perfect bonding between the concrete and FRP strips. This assumption simplifies modeling and analysis, but complete bonding is difficult in real-world applications. Therefore, it is crucial to recognize this assumption as a limitation of the study.
- The model could potentially ignore certain localized impacts or flaws in the FRP-confined column structure. The model might not fully account for discrepancies, site-specific factors, or construction techniques.

Author contributions

Project administration, supervision, Funding Acquisition: **H.F.I.**, Conceptualization, data curation, formal analysis, investigation, methodology, software, validation, visualization, writing—original draft preparation, writing—review and editing: **C.Y., H.F.I., D.N.Q., A.M., T. W., P.J., ARPITA, A.Y.H.** The published version of the manuscript has been read and approved by all authors.

Funding

This research received no external funding.

Declaration of Competing Interest

The authors declares that they have no known competing financial interests or personal relationship that could have appeared to the work reported in this paper.

ANNEXURE I.

Annexure A

Experimental (from literature) and simulated (from parametric study) database of elliptical FRP-confined concrete columns.

Group No.	No.	Source	Specimen	Peak strength of unconfined concrete, f_{co} (MPa)	FRP properties					Geometrical properties			Test results		FEM results	
					Material type	No. of layers	Thickness of layers (mm/mm)	Total thickness, t_f (mm)	Young's modulus, E_f (MPa)	$2a$ (mm)	$2b$ (mm)	H (mm)	f_{cc} (MPa)	ε_{cc} (mm/mm)	f_{cc} (MPa)	ε_{cc} (mm/mm)
A	1	Chen et al.[3]	A1	72.4	CFRP	3	0.167	0.501	210000	250	250	500	104.850	0.0180	105.848	0.0190
	2	Chen et al.[3]	A2	72.4	CFRP	3	0.167	0.501	210000	250	192	500	88.750	0.0163	87.518	0.0147
	3	Chen et al.[3]	A3	72.4	CFRP	3	0.167	0.501	210000	250	147	500	79.000	0.0118	79.881	0.0133
	4	Chen et al.[3]	A4	72.4	CFRP	3	0.167	0.501	210000	250	125	500	76.650	0.0105	73.929	0.0112
	5	Chen et al.[3]	A5	72.4	GFRP	5	0.354	1.770	72000	250	250	500	108.450	0.0152	107.528	0.0154
	6	Chen et al.[3]	A6	72.4	GFRP	5	0.354	1.770	72000	250	192	500	93.900	0.0124	91.331	0.0118
	7	Chen et al.[3]	A7	72.4	GFRP	5	0.354	1.770	72000	250	147	500	83.100	0.0099	82.628	0.0105
	8	Chen et al.[3]	A8	72.4	GFRP	5	0.354	1.770	72000	250	125	500	77.250	0.0088	75.856	0.0091
	9	Chen et al.[3]	A9	72.4	GFRP	7	0.354	2.478	72000	250	250	500	136.550	0.0216	138.002	0.0208
	10	Chen et al.[3]	A10	72.4	GFRP	7	0.354	2.478	72000	250	192	500	112.250	0.0155	114.645	0.0159
	11	Chen et al.[3]	A11	72.4	GFRP	7	0.354	2.478	72000	250	147	500	96.200	0.0114	97.672	0.0122
	12	Chen et al.[3]	A12	72.4	GFRP	7	0.354	2.478	72000	250	125	500	88.050	0.0105	87.543	0.0106
	13	Parametric	A13	72.4	GFRP	6	0.354	2.124	72000	250	250	500	-	-	116.056	0.0160
	14	Parametric	A14	72.4	GFRP	6	0.354	2.124	72000	250	192	500	-	-	105.509	0.0143
	15	Parametric	A15	72.4	GFRP	6	0.354	2.124	72000	250	147	500	-	-	91.963	0.0121
	16	Parametric	A16	72.4	GFRP	6	0.354	2.124	72000	250	125	500	-	-	82.662	0.0106
	17	Parametric	A17	50.0	CFRP	3	0.167	0.501	210000	250	250	500	-	-	108.808	0.0278
	18	Parametric	A18	50.0	CFRP	3	0.167	0.501	210000	250	192	500	-	-	83.682	0.0225
	19	Parametric	A19	50.0	CFRP	3	0.167	0.501	210000	250	147	500	-	-	75.492	0.0239
	20	Parametric	A20	50.0	CFRP	3	0.167	0.501	210000	250	125	500	-	-	63.112	0.0159
	21	Parametric	A21	50.0	GFRP	5	0.354	1.770	72000	250	250	500	-	-	101.631	0.0189
	22	Parametric	A22	50.0	GFRP	5	0.354	1.770	72000	250	192	500	-	-	81.262	0.0160
	23	Parametric	A23	50.0	GFRP	5	0.354	1.770	72000	250	147	500	-	-	65.574	0.0117
	24	Parametric	A24	50.0	GFRP	5	0.354	1.770	72000	250	125	500	-	-	62.090	0.0111
	25	Parametric	A25	50.0	GFRP	7	0.354	2.478	72000	250	250	500	-	-	173.400	0.0266
	26	Parametric	A26	50.0	GFRP	7	0.354	2.478	72000	250	192	500	-	-	130.713	0.238
	27	Parametric	A27	50.0	GFRP	7	0.354	2.478	72000	250	147	500	-	-	90.910	0.0173
	28	Parametric	A28	50.0	GFRP	7	0.354	2.478	72000	250	125	500	-	-	76.543	0.0141
	29	Parametric	A29	50.0	GFRP	6	0.354	2.124	72000	250	250	500	-	-	133.321	0.0227
	30	Parametric	A30	50.0	GFRP	6	0.354	2.124	72000	250	192	500	-	-	104.111	0.0204
	31	Parametric	A31	50.0	GFRP	6	0.354	2.124	72000	250	147	500	-	-	75.233	0.0141
	32	Parametric	A32	50.0	GFRP	6	0.354	2.124	72000	250	125	500	-	-	72.098	0.145
B	33	Teng et al.[12]	B1	32.6	CFRP	1	0.171	0.171	290000	200	200	400	43.450	0.0083	42.789	0.0079
	34	Teng et al.[12]	B2	32.6	CFRP	1	0.171	0.171	290000	200	155	400	41.550	0.0078	41.780	0.0071
	35	Teng et al.[12]	B3	32.6	CFRP	1	0.171	0.171	290000	200	120	400	37.800	0.0049	39.138	0.0058
	36	Teng et al.[12]	B4	32.6	CFRP	1	0.171	0.171	290000	200	100	400	35.500	0.0037	36.770	0.0037
	37	Parametric	B5	32.6	CFRP	1	0.171	0.171	290000	200	80	400	-	-	32.252	0.0017
	38	Teng et al.[12]	B6	46.4	CFRP	1	0.171	0.171	290000	200	200	400	52.600	0.0064	52.929	0.0069
	39	Teng et al.[12]	B7	46.4	CFRP	1	0.171	0.171	290000	200	155	400	51.800	0.0072	55.459	0.0087
	40	Teng et al.[12]	B8	46.4	CFRP	1	0.171	0.171	290000	200	120	400	50.400	0.0064	52.714	0.0064
	41	Teng et al.[12]	B9	46.4	CFRP	1	0.171	0.171	290000	200	100	400	47.450	0.0043	51.668	0.0054
	42	Parametric	B10	46.4	CFRP	1	0.171	0.171	290000	200	80	400	-	-	48.787	0.0032

(*continued on next page*)

Annexure A (*continued*)

Group No.	No.	Source	Specimen	Peak strength of unconfined concrete, f_{co} (MPa)	FRP properties					Geometrical properties			Test results		FEM results	
					Material type	No. of layers	Thickness of layers (mm/mm)	Total thickness, t_f (mm)	Young's modulus, E_f (MPa)	$2a$ (mm)	$2b$ (mm)	H (mm)	f_{cc} (MPa)	ε_{cc} (mm/mm)	f_{cc} (MPa)	ε_{cc} (mm/mm)
	43	Teng et al.[12]	B11	35.8	CFRP	2	0.171	0.342	290000	200	200	400	56.100	0.0119	65.191	0.0156
	44	Teng et al.[12]	B12	35.8	CFRP	2	0.171	0.342	290000	200	155	400	52.100	0.0099	57.643	0.0117
	45	Teng et al.[12]	B13	35.8	CFRP	2	0.171	0.342	290000	200	120	400	58.300	0.0130	59.814	0.0129
	46	Teng et al.[12]	B14	35.8	CFRP	2	0.171	0.342	290000	200	100	400	45.250	0.0086	51.580	0.0089
	47	Parametric	B15	35.8	CFRP	2	0.171	0.342	290000	200	80	400	-	-	45.894	0.0061
	48	Teng et al.[12]	B16	40.2	CFRP	2	0.171	0.342	290000	200	200	400	60.900	0.0091	64.167	0.0103
	49	Teng et al.[12]	B17	40.2	CFRP	2	0.171	0.342	290000	200	155	400	59.350	0.0094	61.738	0.0099
	50	Teng et al.[12]	B18	40.2	CFRP	2	0.171	0.342	290000	200	120	400	56.650	0.0096	62.054	0.0120
	51	Teng et al.[12]	B19	40.2	CFRP	2	0.171	0.342	290000	200	100	400	51.400	0.0082	56.089	0.0098
	52	Parametric	B20	40.2	CFRP	2	0.171	0.342	290000	200	80	400	-	-	48.324	0.0066
C	53	Wang et al.[62]	C1	24.5	CFRP	1	0.171	0.171	290000	305	305	915	35.000	0.0185	35.164	0.0178
	54	Parametric	C2	24.5	CFRP	1	0.171	0.171	290000	305	235	915	-	-	32.873	0.0147
	55	Parametric	C3	24.5	CFRP	1	0.171	0.171	290000	305	180	915	-	-	31.367	0.0115
	56	Parametric	C4	24.5	CFRP	1	0.171	0.171	290000	305	152	915	-	-	28.078	0.0087
	57	Parametric	C5	24.5	CFRP	1	0.171	0.171	290000	305	122	915	-	-	25.974	0.0040
D	58	Liu et al.[49]	D1	41.2	GFRP	6	0.482	2.890	72000	299.5	299.5	600	85.600	0.0273	83.969	0.0267
	59	Liu et al.[49]	D2	41.2	GFRP	6	0.473	2.840	72000	295.9	196.0	600	73.400	0.0244	75.295	0.0244
	60	Liu et al.[49]	D3	41.2	GFRP	6	0.523	3.140	72000	297.9	150.3	600	52.000	0.0199	51.707	0.0201
	61	Liu et al.[49]	D4	41.2	GFRP	6	0.525	3.150	72000	295.8	119.4	600	43.700	0.0215	44.752	0.0216
	62	Liu et al.[49]	D5	53.6	GFRP	6	0.482	2.890	72000	299.5	299.5	600	89.800	0.0219	89.025	0.0218
	63	Liu et al.[49]	D6	53.6	GFRP	6	0.473	2.840	72000	295.9	196.0	600	77.200	0.0206	78.743	0.0206
	64	Liu et al.[49]	D7	53.6	GFRP	6	0.523	3.140	72000	297.9	150.3	600	57.200	0.0166	56.862	0.0169
	65	Liu et al.[49]	D8	53.6	GFRP	6	0.525	3.150	72000	295.8	119.4	600	50.500	0.0149	46.783	0.0148
	66	Liu et al.[49]	D9	53.6	GFRP	10	0.485	4.850	72000	299.5	299.5	600	112.200	0.0241	112.366	0.0238
	67	Liu et al.[49]	D10	53.6	GFRP	10	0.443	4.430	72000	295.9	196.0	600	102.500	0.0256	103.554	0.0256
	68	Liu et al.[49]	D11	53.6	GFRP	10	0.426	4.260	72000	297.9	150.3	600	66.500	0.0158	65.858	0.0157
	69	Liu et al.[49]	D12	53.6	GFRP	10	0.441	4.410	72000	295.8	119.4	600	60.300	0.0148	60.251	0.0148
	70	Liu et al.[49]	D13	75.7	GFRP	1	2.890	2.890	72000	299.5	299.5	600	95.900	0.0084	91.485	0.0085
	71	Liu et al.[49]	D14	75.7	GFRP	1	2.840	2.840	72000	295.9	196.0	600	74.500	0.0102	71.635	0.0103
	72	Liu et al.[49]	D15	75.7	GFRP	1	3.140	3.140	72000	297.9	150.3	600	55.100	0.0096	55.868	0.0092
	73	Liu et al.[49]	D16	75.7	GFRP	1	3.150	3.150	72000	295.8	119.4	600	55.300	0.0086	53.264	0.0094
	74	Parametric	D17	30	GFRP	4	0.354	1.416	72000	299.5	299.5	600	-	-	51.438	0.0214
	75	Parametric	D18	30	GFRP	4	0.354	1.416	72000	295.9	196.0	600	-	-	34.005	0.0142
	76	Parametric	D19	30	GFRP	4	0.354	1.416	72000	297.9	150.3	600	-	-	28.535	0.0138
	77	Parametric	D20	30	GFRP	4	0.354	1.416	72000	295.8	119.4	600	-	-	25.196	0.0122
	78	Parametric	D21	30	GFRP	5	0.354	1.770	72000	299.5	299.5	600	-	-	51.980	0.0201
	79	Parametric	D22	30	GFRP	5	0.354	1.770	72000	295.9	196.0	600	-	-	38.254	0.0172
	80	Parametric	D23	30	GFRP	5	0.354	1.770	72000	297.9	150.3	600	-	-	30.563	0.0140
	81	Parametric	D24	30	GFRP	5	0.354	1.770	72000	295.8	119.4	600	-	-	28.355	0.0130
	82	Parametric	D25	30	GFRP	6	0.354	2.124	72000	299.5	299.5	600	-	-	38.658	0.0236
	83	Parametric	D26	30	GFRP	6	0.354	2.124	72000	295.9	196.0	600	-	-	41.430	0.0189
	84	Parametric	D27	30	GFRP	6	0.354	2.124	72000	297.9	150.3	600	-	-	33.300	0.0156
	85	Parametric	D28	30	GFRP	6	0.354	2.124	72000	295.8	119.4	600	-	-	30.220	0.0136

$2a$ = Longer side of elliptical section (mm); $2b$ = Shorter side of elliptical section (mm); H = Height of concrete column (mm); f_{co} = Peak strength of unconfined concrete column (MPa); f_{cc} = Peak strength of confined concrete column (MPa); ε_{cc} = Peak strain of confined concrete column (mm/mm); FRP = Fiber reinforced polymer; t_f = Total thickness of FRP layers; E_f = Young's modulus of FRP.

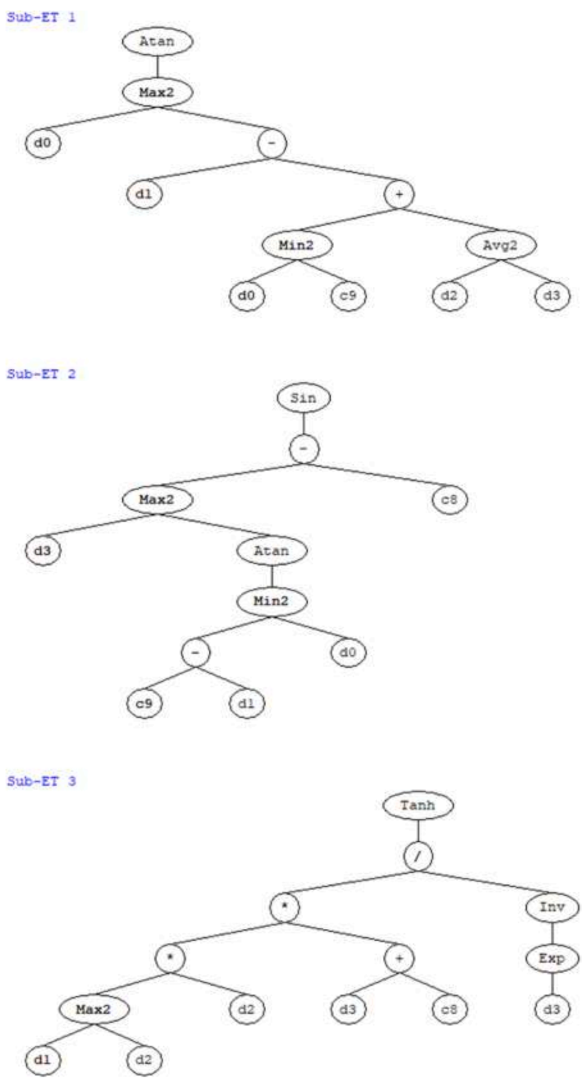

Fig. 28. Expression tree of GEP model.

Table 9
GEP model parameters.

Function	(+ - * /), pow, sqrt, Exp, Ln, Sin, Arctan, Tanh, Max, min, Avg
Number of generations	15000
Chromosomes	2048
Head size	7
Number of genes	3
Linking function	Addition
Mutation	0.044
IS Transposition	0.1
RIS Transposition	0.1
One-point recombination rate	0.2
Two-point recombination rate	0.3
Gene recombination	0.2
Gene transposition	0.1

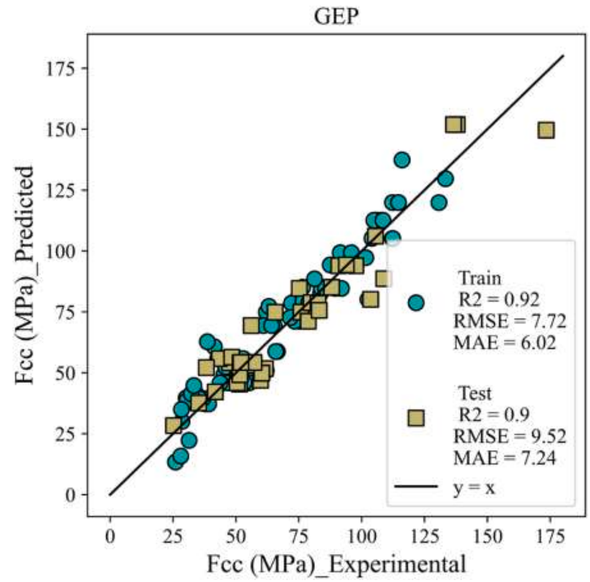

Fig. 29. Result of GEP model.

Data Availability

Data associated with the present study will be available on request from the corresponding author.

References

[1] Liao J, Li YL, Ouyang Y, Zeng JJ. Axial compression tests on elliptical high strength steel tubes filled with self-compacting concrete of different mix proportions. J Build Eng 2021;40:102678.
[2] Zeng JJ, Liang SD, Li YL, Guo YC, Shan GY. Compressive behavior of FRP-confined elliptical concrete-filled high-strength steel tube columns. Compos Struct 2021;266:113808.
[3] Chen G, Wang Y, Yu T, Wan B, Zhang B, Liu Q. Behavior and design-oriented model for elliptical FRP-confined concrete under axial compression. Eng Struct 2021;249:113387. https://doi.org/10.1016/j.engstruct.2021.113387.
[4] Wang J, Cheng A, Shen Q, Li G, Xiao Q. Eccentric compression behaviour and assessment of CFET short columns offering spherical-cap gaps. J Constr Steel Res 2022;197:107476. https://doi.org/10.1016/j.jcsr.2022.107476.
[5] Gao X, Liu Y, Liu Y, Wang D. Experimental and analytical study on compressive bearing capacity of steel shell-concrete composite bridge tower. Eng Struct 2023;278:115567. https://doi.org/10.1016/j.engstruct.2022.115567.
[6] Xu Y, Zheng B, Zhang M. Capacity prediction of cold-formed stainless steel tubular columns using machine learning methods. J Constr Steel Res 2021;182:106682. https://doi.org/10.1016/j.jcsr.2021.106682.
[7] Campione G, Miraglia N. Strength and strain capacities of concrete compression members reinforced with FRP. Cem Concr Compos 2003;25:31–41. https://doi.org/10.1016/S0958-9465(01)00048-8.
[8] Hamed AY, Hassanein MF, Hasan MA. Stress-strain modelling of circular concrete-filled FRP–steel composite tube columns under axial compression load. Structures 2024;67:107040. https://doi.org/10.1016/j.istruc.2024.107040.
[9] Hassanein MF, Hamed AY, Cashell KA, Shao YB. Confinement-based direct design method for fibre reinforced polymer confined CFST short columns. Thin-Walled Struct 2023;192:111207. https://doi.org/10.1016/j.tws.2023.111207.
[10] Shao YB, Hamed AY, Elsisy AR, Hadzima-Nyarko M, Radu D, Hassanein MF. Confinement-based direct design of square normal and high strength steel tube confined concrete (STCC) short columns. Structures 2024;65:106705. 10.1016/j.istruc.2024.106705.
[11] Teng J, Lam L. Compressive behavior of carbon fiber reinforced polymer-confined concrete in elliptical columns. J Struct Eng 2002;128:1535–43.
[12] Teng J, Wu J, Casalboni S, Xiao Q, Zhao Y. Behavior and modeling of fiber-reinforced polymer-confined concrete in elliptical columns,". Adv Struct Eng 2016;19:1359–78.
[13] Teng J, Jiang T, Lam L, Luo Y. Refinement of a design-oriented stress–strain model for FRP-confined concrete. J Compos Constr 2009;13:269–78.
[14] Wei YY, Wu YF. Unified stress–strain model of concrete for FRP-confined columns. Constr Build Mater 2012;26:381–92.
[15] Cao YG, Jiang C, Wu YF. Cross-sectional unification on the stress-strain model of concrete subjected to high passive confinement by fiber-reinforced polymer. Polymers 2016;8:186.
[16] Lam L, Teng J. Strength models for fiber-reinforced plastic-confined concrete. J Struct Eng 2002;128:612–23.

[17] Teng J, Xiao Q, Yu T, Lam L. Three-dimensional finite element analysis of reinforced concrete columns with FRP and/or steel confinement. Eng Struct 2015; 97:15–28.
[18] Chellapandian M, Prakash SS, Sharma A. Experimental and finite element studies on the flexural behavior of reinforced concrete elements strengthened with hybrid FRP technique. Compos Struct 2019;208:466–78.
[19] Li Y, Zhao XL, Raman RS. Theoretical model for concrete-filled stainless steel circular stub columns under axial compression. J Constr Steel Res 2019;157: 426–39.
[20] Yu T, Zhao H, Ren T, Remennikov A. Novel hybrid FRP tubular columns with large deformation capacity: Concept and behaviour. Compos Struct 2019;212:500–12.
[21] Mohammadi M, Bai YL, Yang HL, Lin G, Dai JG, Zhang YF. FE modeling of Non-circular LRS FRP-confined concrete columns. Compos Struct 2022;286:115314.
[22] Hassanein MF, Silvestre N, Yan XF. Confinement-based direct design of circular concrete-filled double-skin normal and high strength steel short columns. Thin-Walled Struct 2023;183:110446.
[23] Isleem HF, Wang Z, Wang D, Smith ST. "Monotonic and cyclic axial compressive behavior of CFRP-confined rectangular RC columns,". J Compos Constr 2018;22: 04018023. https://doi.org/10.1061/(ASCE)CC.1943-5614.0000860.
[24] Isleem HF, Wang D, Wang Z. A new numerical model for polymer-confined rectangular concrete columns. Proc Inst Civ Eng-Struct Build 2019;172:528–44.
[25] Isleem HF, Tahir M, Wang Z. Axial stress–strain model developed for rectangular RC columns confined with FRP wraps and anchors. Structures 2020;23:779–88.
[26] Isleem HF, Peng F, Tayeh BA. "Confinement model for LRS FRP-confined concrete using conventional regression and artificial neural network techniques. Compos Struct 2022;279:114779.
[27] Isleem HF, Wang D, Wang Z. Modeling the axial compressive stress-strain behavior of CFRP-confined rectangular RC columns under monotonic and cyclic loading. Compos Struct 2018;185:229–40.
[28] Zhang B, Feng GS, Wang YL, Lai CC, Wang CC, Hu XM. Elliptical FRP-concrete-steel double-skin tubular columns under monotonic axial compression. Adv Polym Technol 2020:1–16.
[29] Isleem HF, Wang Z. Axial compressive stress-strain model developed for FRP-confined concrete columns with elliptical cross sections. J Compos Sci 2018;67(2).
[30] Ozbakkaloglu T, Gholampour A, Lim JC. "Damage-plasticity model for FRP-confined normal-strength and high-strength concrete. J Compos Constr 2016;20: 04016053.
[31] Hassanein MF, Hamed AY, Shao YB, Silvest N. "Confinement-based direct design of circular steel tube confined concrete (STCC) short columns. J Constr Steel Res 2023;204:107871. https://doi.org/10.1016/j.jcsr.2023.107871.
[32] Hamed AY. "Elastic shear buckling of tapered steel plate girders with opening in web. J Eng Sci (JES) 2023;51(3):148–72. https://doi.org/10.21608/JESAUN.2023.177464.1184.
[33] Mohammadi M, Wu YF. Triaxial test for concrete under non-uniform passive confinement. Constr Build Mater 2017;138:455–68.
[34] Isleem HF, Peng F, Tayea BA. Artificial Neural Network (ANN) and Finite Element (FE) Models for Simulating the Axial Compression Behavior of GFRP RC Columns,". DOI: 10.3390/ma14237172 Mater MDPI 2021. DOI: 10.3390/ma14237172.
[35] Isleem HF, Tayeh BA, Abid M, Iqbal M, Mohamed AM, Sherbiny ME. Finite element and artificial neural network modeling of FRP-RC columns under axial compression loading (p. Frontiers in Materials) Front Mater 2022;9 (p. Frontiers in Materials).
[36] Chen G, Wang Y, Yu T, Zhang B, Han B. "Elliptical FRP–concrete–steel double-skin tubular columns: axial behavior, interaction mechanism, and modeling. J Compos Constr 2022;26:04022078.
[37] Hany NF, Hantouche EG, Harajli MH. Finite element modeling of FRP-confined concrete using modified concrete damaged plasticity. Eng Struct 2016;125:1–14.
[38] J.C. Lim, T. Ozbakkaloglu, A. Gholampour, T. Bennett and R. Sadeghi, "Finite-element modeling of actively confined normal-strength and high-strength concrete under uniaxial, biaxial, and triaxial compression," Journal of Structural Engineering, vol. 142, p. 04016.
[39] Mazzucco G, Salomoni V, Majorana C, Pellegrino C, Ceccato C. Numerical investigation of concrete columns with external FRP jackets subjected to axial loads. Constr Build Mater 2016;111:590–9.
[40] Altalabani D, Hejazi F, Rashid RB, Abd Aziz FN, F.N.A. Development of new rectangular rubber isolators for a tunnel-form structure subjected to seismic excitations. Structures 2021;32:1522–42.
[41] Jiang JF, Wu YF. "Characterization of yield surfaces for FRP-confined concrete. J Eng Mech 2014;140:04014096.
[42] Liu K, Jiang C, Yu T, Teng J. "Compressive behaviour of elliptical FRP tube-confined concrete columns. Compos Struct 2023;303:116301.
[43] Wu F, Tang F, Lu R, Cheng M. "Predicting compressive strength of RCFST columns under different loading scenarios using machine learning optimization. Sci Rep 2023;13:16571.
[44] Naderpour H, Kheyroddin A, Amiri GG. "Prediction of FRP-confined compressive strength of concrete using artificial neural networks,". Compos Struct 2010;92: 2817–29.
[45] Huang L, Chen J, Tan X. "BP-ANN based bond strength prediction for FRP reinforced concrete at high temperature. Eng Struct 2022;257:114026.
[46] Alam MS, Gazder U. "Shear strength prediction of FRP reinforced concrete members using generalized regression neural network. Neural Comput Appl 2020; 32:6151–8.
[47] Kim B, Lee DE, Hu G, Natarajan Y, Preethaa S, Rathinakumar AP. Ensemble machine learning-based approach for predicting of FRP–concrete interfacial bonding. Mathematics 2022;10:231.
[48] Sangeetha P, Shanmugapriya M. GFRP wrapped concrete column compressive strength prediction through neural network. SN Appl Sci 2020;2:1–11.
[49] C. Xu, Y. Zhang, H.F. Isleem, D. Qiu, Y. Zhang, M.M. Alsaadawi, R.K. Tipu, W.E. El-Demerdash and A.Y. Hamed, "Numerical and machine learning models for concentrically and eccentrically loaded CFST columns confined with FRP wraps," Structural Concrete, p. ⟨https://doi.org/10.1002/suco⟩. 202400541, 2024.
[50] Isleem HF, Qiong T, Chukka NR, Kumar R, Nagaraju TV, Hamed AY. Machine learning and nonlinear finite element analysis of fiber-reinforced polymer confined concrete-steel double-skin tubular columns under axial compression. Struct Concr 2024:1–24. https://doi.org/10.1002/suco. 202300835.
[51] Zhao C, Zhong J, Wang H, Liu C, Li M, Liu H. Impact behaviour and protectionperformance of a CFRP NPR skeleton filled withaluminum foam. Mater Des 2024:113295. https://doi.org/10.1016/j.matdes.2024.113295.
[52] Wang Z, Wang D, Smith ST, Lu D. Experimental testing and analytical modeling of CFRP-confined large circular RC columns subjected to cyclic axial compression. Eng Struct 2012;40:64–74.
[53] ABAQUS Standard., "User's manual the Abaqus software is a product of Dassault systems Simulia Corp," USA Dassault systems version 6.14, Providence, RI., 2014.
[54] Vahidpour M, Kheyroddin A, Kioumarsi M. Experimental investigation on flexural capacity of reinforced concrete beams strengthened with 3D-fiberglass, CFRP and GFRP. Int J Concr Struct Mater 2022;16:1–20.
[55] T. Yu, J. Teng, Y. Wong and S. Dong, "Finite element modeling of confined concrete-I: Drucker–Prager type plasticity model," Engineering structures, vol. 32, pp. 665–679, 210.
[56] Yu T, Teng J, Wong Y, Dong S. Finite element modeling of confined concrete-II: Plastic-damage model. Eng Struct 2010;32:680–91.
[57] Ferrotto F, Fischer O, Cavaleri L. A strategy for the finite element modeling of FRP-confined concrete columns subjected to preload,". Eng Struct 2018;173:1054–67. https://doi.org/10.1016/j.engstruct.2018.07.047.
[58] S. Michał and W. Andrzej, "Calibration of the CDP model parameters in Abaqus.," World Congr Adv Struct Eng Mech (ASEM 15), Incheon Korea, 2015.
[59] Papanikolaou VK, Kappos AJ. Confinement-sensitive plasticity constitutive model for concrete in triaxial compression. Int J Solids Struct 2007;44(21):7021–48.
[60] Tao Z, Wang ZB, Yu Q. Finite element modelling of concrete-filled steel stub columns under axial compression. J Constr Steel Res 2013;89:121–31.
[61] Isleem HF, K. C. N.D, Bahrami A, Kumar R, Sor NH. Nonlinear finite element and machine learning modelling of tubed reinforced concrete columns under eccentric axial compression loading. DOI: 10.1002/suco.202300835 Alex Eng J 2024. DOI: 10.1002/suco.202300835.
[62] Isleem HF, et al. "Finite element, analytical, artificial neural network models for carbon fibre reinforced polymer confined concrete filled steel columns with elliptical cross sections. Front Mater 2023;9:1115394.
[63] Ho JC, Ou XL, Chen MT, Wang Q, Lai MH. A path dependent constitutive model for CFFT column. Eng Struct 2020;210:110367. https://doi.org/10.1016/j.engstruct.2020.110367.
[64] Lai MH, Liang YW, Wang Q, Ren FM, Chen MT, Ho JC, J.C.M. A stress-path dependent stress-strain model for FRP-confined concrete. Eng Struct 2020;203: 109824. https://doi.org/10.1016/j.engstruct.2019.109824.
[65] Lai MH, Song W, Ou XL, Chen MT, Wang Q, Ho JC. A path dependent stress-strain model for concrete-filled-steel-tube column. Eng Struct 2020;211:110312. https://doi.org/10.1016/j.engstruct.2020.110312.
[66] Dong CX, Kwan AK, Ho JC. A constitutive model for predicting the lateral strain of confined concrete. Eng Struct 2015;91:155–66. https://doi.org/10.1016/j.engstruct.2015.02.014.
[67] Kwan AK, Dong CX, Ho JC. Axial and lateral stress–strain model for FRP confined concrete. Eng Struct 2015;99:285–95. https://doi.org/10.1016/j.engstruct.2015.04.046).
[68] Lai M, Hanzic L, Ho JC. Fillers to improve passing ability of concrete. Struct Concr 2019;20(1):185–97. https://doi.org/10.1002/suco.201800047.
[69] Lai MH, Binhowimal SM, Griffith AM, Hanzic L, Wang Q, Chen Z, Ho JM. Shrinkage design model of concrete incorporating wet packing density. Constr Build Mater 2021;280:122448. https://doi.org/10.1016/j.conbuil.
[70] Lai MH, Binhowimal SA, Griffith AM, Hanzic L, Chen Z, Wang Q, Ho JM. Shrinkage, cementitious paste volume, and wet packing density of concrete. Struct Concr 2022;23(1):488–504. https://doi.org/10.1002/suco.20200040.
[71] Aslani F, Jowkarmeimandi R. Stress–strain model for concrete under cyclic loading. Mag Concr Res 2012;64:673–85.
[72] ACI, ACI 318–14, "Building Code Requirements for Structural Concrete and Commentary," American Concrete Institute (ACI), Farmington Hills, MI, 2014.
[73] Cui C, Sheikh S. Analytical model for circular normal-and high-strength concrete columns confined with FRP. J Compos Constr 2010;14:562–72.
[74] Vincent T, Ozbakkaloglu T. Influence of concrete strength and confinement method on axial compressive behavior of FRP confined high-and ultra high-strength concrete. Compos Part B: Eng 2013;50:413–28.
[75] Isleem HF, Yusuf BO, Xingchong W, Qiong T, Jagadesh P, Augustino DS. Analytical and numerical investigation of polyvinyl chloride (PVC) confined concrete columns under different loading conditions. Aust J Struct Eng 2023;25(1):69–97. https://doi.org/10.1080/13287982.2023.2216566.
[76] Isleem HF, Jagadesh P, Qaidi S, Althoey F, Rahmawati C, Najm HM, Sabri MS. Finite element and theoretical investigations on PVC–CFRP confined concrete columns under axial compression. Front Mater 2022;9. https://doi.org/10.3389/fmats.2022.1055397.
[77] Mansourdehghan S, Dolatshahi KM, Asjodi A. Data-driven damage assessment of reinforced concrete shear walls using visual features of damage. J Build Eng 2022; 53:104509.

[78] Tajik N, Mahmoudian A, Taleshi M, Yekrangnia M. Explainable XGBoost machine learning model for prediction of ultimate load and free end slip of GFRP rod glued-in timber joints through a pull-out test under various harsh environmental conditions. Asian J Civ Eng 2024;25(1):141–57.

[79] Mahmoudian A, Tajik N, Taleshi MM, Shakiba M, Yekrangnia M. Ensemble machine learning-based approach with genetic algorithm optimization for predicting bond strength and failure mode in concrete-GFRP mat anchorage interface. Structures 2023;57:105173.

[80] L.S. Shapley, "A value for n-person games," 1953.

[81] Mangalathu S, Hwang SH, Jeon JS. Failure mode and effects analysis of RC members based on machine-learning-based SHapley Additive exPlanations (SHAP) approach. Eng Struct 2020;219:110927.

[82] Taleshi MM, Tajik N, Mahmoudian A, Yekrangnia M. Prediction of pull-out behavior of timber glued-in glass fiber reinforced polymer and steel rods under various environmental conditions based on ANN and GEP models. Case Stud Constr Mater 2024;20:e02842.

[83] Chen L, Fakharian P, Eidgahee DR, Haji M, Arab AM, Nouri Y. Axial compressive strength predictive models for recycled aggregate concrete filled circular steel tube columns using ANN, GEP, and MLR. J Build Eng 2023;77:107439.